Precision Engineering 72 (2021) 502–520

Contents lists available at ScienceDirect

Precision Engineering

journal homepage: www.elsevier.com/locate/precision

Shaking force balancing of a 2-DOF isotropic horological oscillator

H. Schneegans *, E. Thalmann, S. Henein

Micromechanical and Horological Design Laboratory (Instant-Lab), École Polytechnique Fédérale de Lausanne (EPFL), Neuchâtel, Switzerland

ARTICLE INFO

Keywords:
Compliant mechanisms
Shaking force balancing
Dynamic balancing
2-DOF Mechanism
Mechanical oscillator
Silicon flexures

ABSTRACT

Despite centuries of research and significant advances, the escapement mechanism used to count and maintain oscillations of mechanical time bases remains a complex mechanism and a major source of energy losses. We showed in previous work that, instead of the widely used rotational one degree-of-freedom (DOF) oscillators, 2-DOF flexure oscillators have the potential of revolutionizing mechanical watchmaking by eliminating the traditional escapement, replacing it by a simple crank driving a pin. Additionally, using flexures increases the quality factor of the time base, leading to further potential improvements in timekeeping accuracy and energy consumption. However, a significant challenge of these new time bases is their balancing such that the influence of external accelerations on their frequency is minimized, a necessary condition for accurate timekeeping in portable applications. This article presents a novel 2-DOF planar flexure oscillator called Wattwins and demonstrates how it can be made insensitive to linear accelerations such as gravity. For this purpose, a new approach to shaking force balancing is developed based on the decomposition of perturbations into effects corresponding to different orders of center of mass displacement. A full analytical model for frequency tuning and shaking force balancing of the 2-DOF oscillator is derived using a pseudo-rigid-body model and assuming that it can be decomposed into two independent 1-DOF oscillators. The results are validated by the finite element method and show that practical mechanical watch specifications can theoretically be reached. A physical prototype was also constructed and preliminary experimental results confirm the theory as well as the simulations.

1. Introduction

1.1. The IsoSpring concept

High chronometric accuracy and long power reserve (i.e., high efficiency) have become the most important performance requirements of modern mechanical watches. The recent developments of silicon flexure oscillators have allowed to significantly increase the quality factor of the time base in comparison to traditional balance wheel and hairspring oscillator [1,2]. This paves the way to significant improvements in accuracy and efficiency since the quality factor quantifies the energy losses of the time base and is considered to be a direct indicator of timekeeping accuracy [3]. The next step in increasing mechanical watch efficiency is to address the efficiency of the escapement mechanism, which does not exceed 40% for the lever escapement used in most mechanical watches. This significant power loss results from shocks and friction between parts during the stop-and-go motion of this mechanism, see Fig. 1 [4].

The *IsoSpring* mechanical time base solves the efficiency issue of the escapement by completely eliminating it with the introduction of the 2-DOF oscillator [5,6]. This isotropic harmonic oscillator, where a point mass m at position r is subject to a central linear restoring force (Hooke's law), was first described in 1687 by Isaac Newton in Principia Mathematica [7]. The resulting trajectories depicted in Fig. 2a are elliptical and isochronous, that is, the frequency of rotation is the same for all orbits. Since isochronism is the basis of precision timekeeping, oscillators based on this concept are ideal candidates as time bases for mechanical timekeepers. The most interesting property of this oscillator is that its motion is unidirectional, as opposed to the back and forth motion of existing mechanical time bases. As a result, the problem of inefficiency of the escapement is solved by eliminating it completely since there is no more stop-and-go motion. In practice, Fig. 2b depicts how the escapement mechanism is replaced by a crank c driven by the energy storage mechanism, such as a watch mainspring, that maintains and counts time base oscillations by a pin p attached to the oscillator.

1.2. The Wattwins oscillator

In theory, the IsoSpring could be implemented such as described in

* Corresponding author.
E-mail addresses: hubert.schneegans@epfl.ch (H. Schneegans), etienne.thalmann@epfl.ch (E. Thalmann), simon.henein@epfl.ch (S. Henein).

https://doi.org/10.1016/j.precisioneng.2021.06.003
Received 29 December 2020; Received in revised form 31 May 2021; Accepted 8 June 2021
Available online 25 June 2021

Fig. 2. In practice, however, the moving mass has a non-zero inertia which results in an isochronism defect [5]. This problem can be solved by having the mass translate on its elliptical orbit without rotating, hence eliminating the effect of its inertia. This can be implemented by constraining the motion of the mass to planar translations and coupling it in parallel to two orthogonal springs providing an isotropic linear central restoring force. As proof-of-concept, we embodied this idea in a flexure-based planar IsoSpring [6] and used it as time base for a mechanical clock.[1]

The planar clock oscillator successfully showed that the IsoSpring enables eliminating the escapement but this oscillator cannot be used for portable timekeepers, such as watches, which are the ultimate target of this invention. Indeed, this oscillator is very sensitive to linear accelerations (such as gravity) and can hence only operate in a horizontal plane. For this reason, a new 2-DOF planar mechanical oscillator called *Wattwins* was developed whose architecture is based on two orthogonal Watt linkages, each realizing one DOF in translation (thick black lines on Fig. 3a). We showed that this oscillator could be implemented at watch scale with a silicon flexure prototype, see Fig. 4a, and that it could successfully be driven by a watch movement, see Fig. 4 and video [8]. The Wattwins architecture was chosen for its potential to be insensitive to linear and angular accelerations. We already showed in previous work [9] how to dynamically balance for small amplitudes an ideal Watt oscillator (Watt's linkage with torsion springs at each joint) and how to tune its eigenfrequency. However, when a coupler is added between the two Watt oscillators (thin red lines on Fig. 3), balancing the system becomes a significantly more complex task. Moreover, matching the eigenfrequencies of the two DOFs, an essential condition for elliptical orbits and oscillator stability, also becomes a greater challenge. These two issues, which need to be solved before implementation in a watch, are the main topic of this article.

Remark 1.1. A different implementation of the IsoSpring using 2-DOF in rotation instead of translations was also studied [10] and demonstrated on a mechanical clock.[2] This oscillator architecture is however considered too sensitive to angular accelerations for portable applications.

1.3. Oscillator balancing

Definition: An oscillator is *shaking force balanced* if its linear momentum is constant for all movements over its workspace [11,12]. Necessarily, the potential energy of the oscillator is then independent of all linear accelerations. The shaking force balanced oscillator is then insensitive to all linear accelerations and does not export any forces to its frame [13].

Definition: An oscillator is *shaking moment balanced* if its angular momentum is constant for all movements over its workspace [11,12]. The shaking moment balanced oscillator is then insensitive to all purely angular accelerations and does not export any torques to its frame [13].

Definition: An oscillator is *dynamically balanced* if it is shaking force balanced and shaking moment balanced [11,12]. The dynamically balanced oscillator is then insensitive to all linear and angular accelerations over its workspace.

The perfect shaking force and shaking moment balancing of a mechanism, also called complete or full shaking force and shaking moment balancing, often considerably increases the complexity of its final design with an inevitable increase of its total mass [14]. Hence, partial shaking force and shaking moment balancing are wildly used, where exported forces and torques are minimized instead of perfectly cancelled. A common approach is to extract the harmonics of the displacement components of a mechanism's center of mass (COM) and to cancel the dominant ones using well located counterweights or additional mechanisms. Similar approaches exist to minimize the shaking moment of a mechanism [13,14].

While shaking force and shaking moment balancing has been largely investigated in the field of rigid body linkages through the last century, little work has been done in the field of compliant mechanisms. Weeke et al. [15] designed and manufactured a fully compliant shaking force balanced mechanical oscillator using the well-known method of linearly independent vectors [16] to compute and fix the position of the structure's COM. Their final design is a 1-DOF double crank slider mechanism having opposite movements that are fully symmetrical, hence fixing the position of the COM. Symmetrizing structures makes it possible to balance them fully at the cost of having a bulkier implementation. This method is hence not scalable when it comes to initially complex mechanisms. Martinez et al. [17] addressed the shaking force balancing of a compliant leaf-spring table using counterweights mounted on flexures. Equalizing the eigenfrequency of the compliant leaf-spring table and the eigenfrequency of the counterweights was the key to reach shaking force balancing as the motion of the counterweights was not geometrically

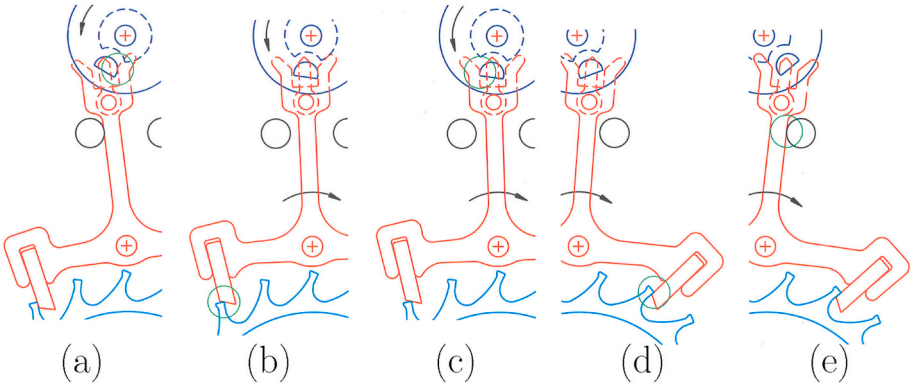

Fig. 1. Shocks during the operation of the Swiss lever escapement: (a) Unlocking, (b) start of impulse by the wheel, (c) start of the balance impulse, (d) end of drop, (e) run to the banking [4].

[1] The working principle of the planar IsoSpring and the operation of the clock can be seen in this video: https://youtu.be/e77FbrBCXqI?t=47.

[2] The operation of the mechanical clock with spherical IsoSpring can be seen in this video: https://youtu.be/nkScUzJ0YVU.

imposed. However, the shaking force balancing of their structure is only valid when it vibrates at its first eigenfrequency. Indeed, if the latter is subjected to any external in-plane accelerations, the shaking force balancing conditions will no longer be respected.

Since the existing shaking force balancing methods are not satisfactory for complex compliant mechanism, we developed a new approach. Note that this article focuses only on shaking force balancing, and not shaking moment balancing, for the following reasons:

- Linear accelerations are the main source of perturbation on mechanical watches (gravity is always present whereas angular accelerations are transient).
- The Wattwins architecture is intrinsically shaking moment balanced to a first approximation, see Section 2.1.
- Current mechanical watches achieve sufficient timekeeping performance even though their time base is not shaking moment balanced.

In theory, the shaking force balancing of a structure is achieved when its potential energy is independent of all linear accelerations. Observe that this definition for shaking force balancing is different from the *static balancing* notion. A mechanism is called statically balanced if its total potential energy is invariant over its workspace [18]. For example, springs can be used to compensate gravity effects without using counterweights and vice versa [19,20]. Compliant mechanisms can also be designed such that their total elastic potential energy stays constant over their range of motion, i.e., their spring stiffness is cancelled [21]. However, such systems are necessarily dependent on linear accelerations (and the orientation of gravity), hence not shaking force balanced.

The present article focuses on making a 2-DOF compliant mechanism shaking force balanced. This will not result in a static balancing of the structure. Indeed, by making its gravitational potential energy constant, the variations in potential energy of the system only correspond to changes in elastic potential energy. This ensures that the mechanism functions as an oscillator with constant stiffness, regardless of linear accelerations or changes in the orientation of gravity. This is equivalent to cancelling the effect of gravity loads on the effective bending stiffness of the flexures, an effect known as stress stiffening. Indeed, a constant gravitational potential energy means that there is no work of gravity during the motion. The equivalence between the energetic and beam theory approaches is discussed by Kahrobaiyan et al. [22] and Thalmann [2, Chapter 6].

The shaking force balancing of a structure is equivalent to having the position of its COM stay constant over its entire workspace. However, this condition cannot always be perfectly fulfilled in practice so, instead, the level of precision required can be defined by the application. Let us take the example of a 1-DOF flexure mechanism. Since flexures have a limited range of motion, the displacement of its COM G along the x-axis multiplied by its total mass M can be expressed using series expansion with three coefficients A, B and C:

$$\vec{MO}\ G{\cdot}\vec{x} = Aq_i + Bq_i^2 + Cq_i^3 + \mathcal{O}\left(q_i^4\right) \tag{1}$$

where q_i (unit: m) is the motion parameter of the 1-DOF structure. Since gravity is the main perturbation this article focuses on, using Eq. (1), the gravitational potential energy of the structure, when $\vec{g}$ is along the x-axis is:

$$V_g = -\vec{MO}\ G{\cdot}\vec{g} = -\left(Aq_i + Bq_i^2 + Cq_i^3 + \mathcal{O}\left(q_i^4\right)\right)g \tag{2}$$

Using Eq. (2), the static effect of gravity on the structure is then given by

$$F = -\frac{\partial V_g}{\partial q_i} = \left(A + 2Bq_i + 3\ Cq_i^2 + \mathcal{O}\left(q_i^3\right)\right)g \tag{3}$$

One can see in Eq. (3) that the different orders of displacement coefficients affect the structure differently when subjected to linear accelerations: the first order coefficient A creates a disruptive force $A \cdot g$ (unit: N), the second order coefficient B creates a disruptive stiffness $2B \cdot g$ (unit: N m^{-1}), the third order coefficient C creates a disruptive quadratic stiffness $3\ C \cdot g$ (unit: N m^{-2}) and so on.

As a result, cancelling the first order displacement coefficient A inhibits the action of external linear accelerations on the structure when it is at its rest position, i.e., it cannot be excited externally. This level of balancing is sufficient for most applications. In a watchmaking context, it is crucial to minimize the effect of linear accelerations on the effective stiffness of the oscillator since it directly impacts its frequency and hence its chronometric stability. The goal is hence the partial shaking force balancing of the structure up to the second order by cancelling the two first A and B coefficients. Note that since displacements and accelerations (gravity) are small, it is assumed that third order effects are negligible for the required precision level.

This way of decomposing the effect of linear accelerations on compliant mechanisms is new and allows to radically change the way we measure their balancing. In the literature, the shaking force balancing of a system is typically evaluated by mounting it on force sensors and measuring the linear forces exported during its motion [15,23,24]. Alternatively, the system is mounted on a compliant stage or floating platform whose excitation by the exported forces is observed [17,25,26]. In Section 3, we explain how, by measuring the sag and the frequency variation of a compliant mechanism subjected to different linear acceleration orientations, it is possible to assess its shaking force balancing up

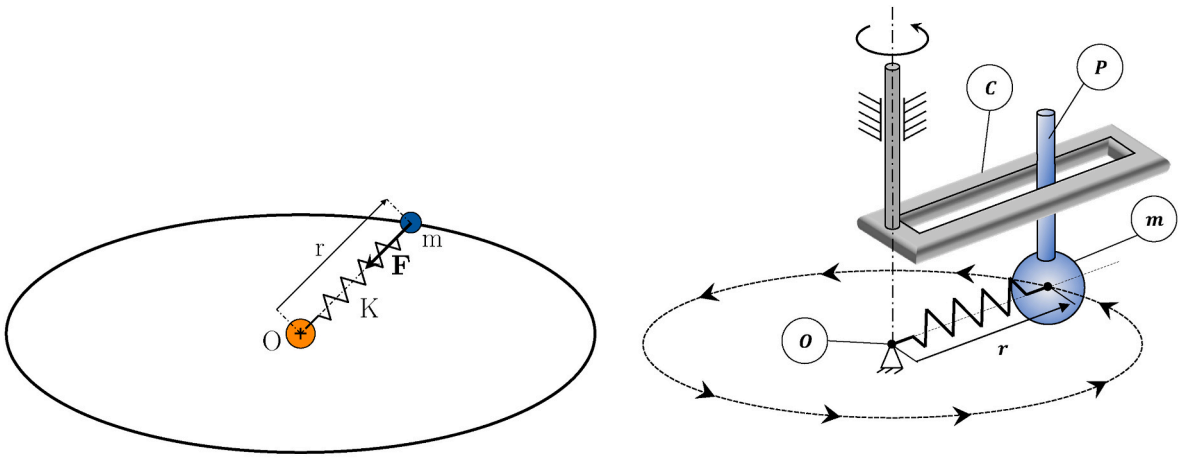

(a) Elliptical orbit under central Hooke's law. (b) An isotropic harmonic oscillator driven by a crank.

Fig. 2. Free and driven isotropic harmonic oscillator.

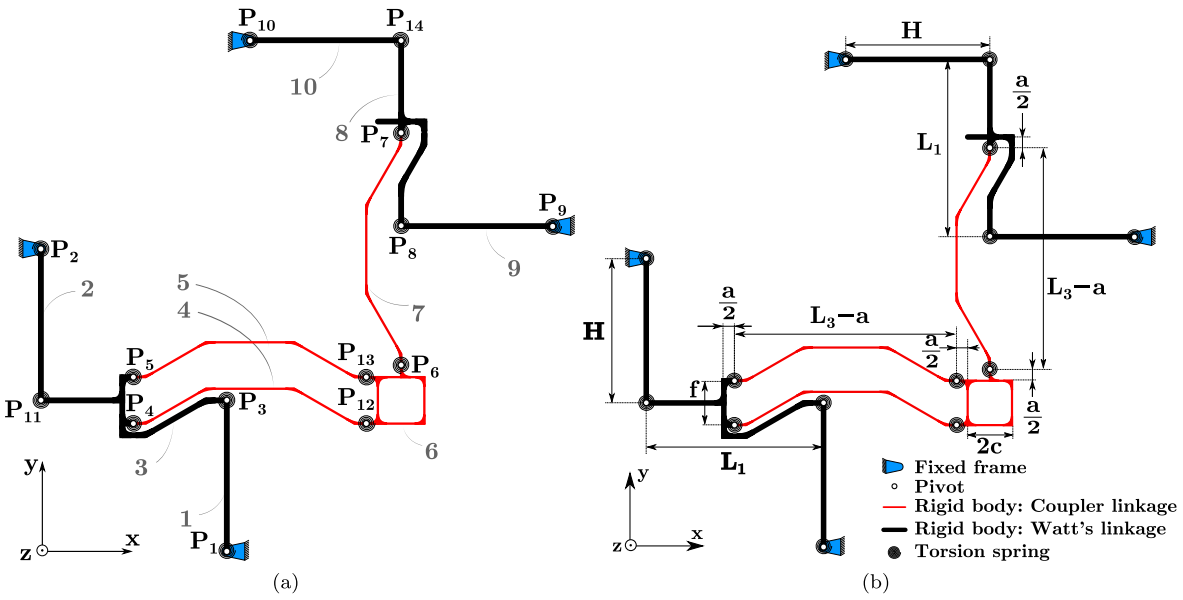

Fig. 3. Pseudo-Rigid-Body Model (PRBM) of the Wattwins oscillator with a) labels for the joints and rigid bodies and b) main geometrical parameters.

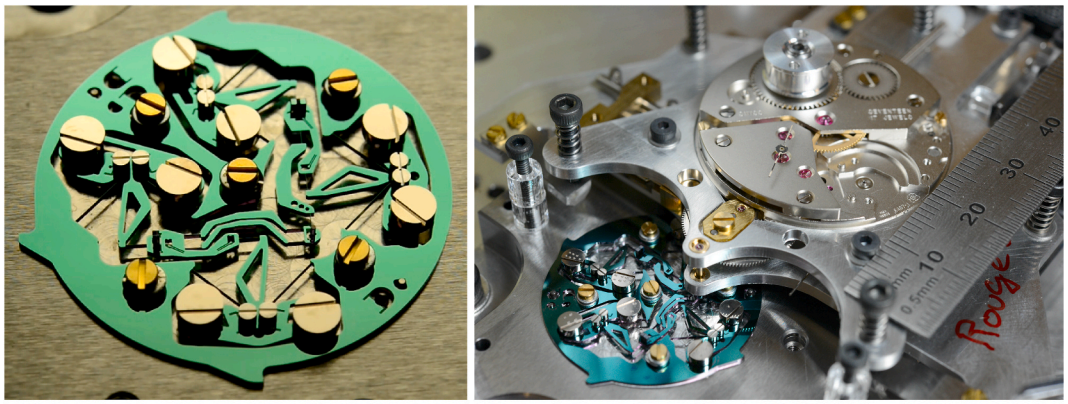

Fig. 4. (a) Centimeter-scale silicon Wattwins oscillator (outer diam. 30 mm) and (b) driving of the Wattwins silicon oscillator with a mechanical watch movement. Video available [8].

to the second order.

Remark 1.2. Solutions to minimize the effect of gravity on the effective stiffness (and thus frequency) of flexure oscillators have already been proposed for the tuning fork [27] and flexure pivot oscillators [2, 22,28,29]. These solutions however concern 1-DOF oscillators and are not directly applicable here.

1.4. Goal and structure of the article

Our goal is to match and tune the eigenfrequencies of the Wattwins oscillator while shaking force balancing it up to the second order in order to minimize the impact of gravity on these frequencies. In Section 2 we describe the pseudo-rigid-body model (PRBM) [30] of the Wattwins architecture and a physical implementation that will be used to validate our results numerically and experimentally. We introduce a decomposition of the Wattwins oscillator into two independent oscillators, the oscillators I and II translating respectively along the x and y axes, that will be used in our analytical model. Section 3 presents the analytical model used to compute the frequencies of oscillators I and II as well as the motion of their COM. Equations are derived for the matching of the two oscillator frequencies and the cancelling of their COM motion up to the second order using the tuning masses. Section 4 validates the analytical model of Section 3 using the finite element method (FEM). We show that shaking force balancing and frequency tuning can be performed independently and that the results match the predictions of the analytical model. Finally, Section 5 presents preliminary experimental results that validate the analytical model for the first order shaking force balancing.

2. Design and kinematics of the Wattwins oscillator

2.1. Design and concept

The PRBM of the Wattwins oscillator is presented in Fig. 3. Its architecture is based on two 1-DOF Watt oscillators arranged at 90° (thick black lines) connected in parallel by a coupler linkage (thin red lines). The first Watt oscillator, whose nearly straight line motion is along the x-axis, consists of two outer rigid bodies of equal length **1** and **2** each connected to the fixed frame at one end with respective pivots $\mathbf{P_1}$ and $\mathbf{P_2}$ and to a middle bar **3** at the other end with respective pivots $\mathbf{P_3}$ and $\mathbf{P_{11}}$. Note that the oscillator's inertia is largely concentrated on the outer rigid bodies **1** and **2**, see Fig. 5. The second Watt oscillator, whose nearly straight line motion is along the y-axis, follows the same architecture as

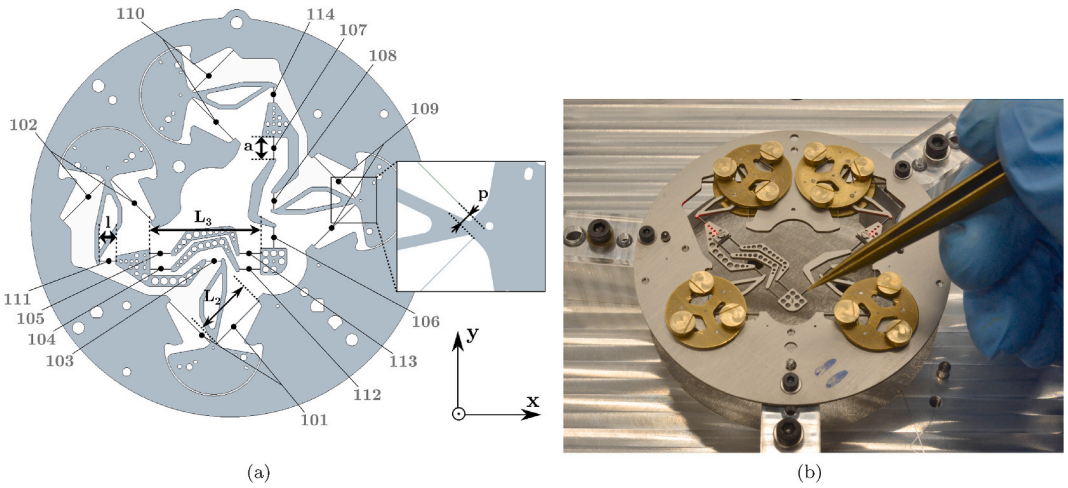

Fig. 5. (a) Wattwins flexure plate and (b) assembled physical titanium oscillator prototype (outer diam. 75 mm).

the first one, with outer rigid bodies **9** and **10**, middle bar **8** and pivots $\mathbf{P_8}$, $\mathbf{P_9}$, $\mathbf{P_{10}}$, $\mathbf{P_{14}}$. The coupler consists of a rigid body **6** connected to the middle bar of the first Watt oscillator by two parallel rigid bodies **4** and **5** and to the middle bar of the second Watt oscillator by rigid body **7**. Each of these rigid bodies have a pivot at each end, respectively $\mathbf{P_4}$ and $\mathbf{P_{12}}$, $\mathbf{P_5}$ and $\mathbf{P_{13}}$, $\mathbf{P_6}$ and $\mathbf{P_7}$. The coupler allows to connect the two Watt oscillators without overconstraint in the plane of the structure,[3] resulting in a 2-DOF planar motion of rigid body **6**. This body holds the driving pin *p* that performs an elliptical motion and is used to drive the mechanism, see Fig. 2b.

In order for this system to act as a mechanical oscillator, spring components must be added. This happens naturally in the flexure implementation of the pivot joints and is represented by the torsion springs coupled to each pivot of the PRBM in Fig. 3 [30,32]. The other essential component of a mechanical oscillator, the inertia, is concentrated on the outer rigid bodies of the two Watt oscillators in order to reach dynamic balancing, see Figs. 4a and 5b. Indeed, one of the main advantages of the Watt oscillator is that the two outer rigid bodies (**1**-**2** and **9**-**10**) rotate in opposite directions. Hence, dividing the inertia of the oscillator equally between these two elements makes it possible to cancel the in-plane angular momenta, i.e., to reach shaking moment balancing in the oscillator plane. Note that this is a first order approximation valid only in the plane of the oscillator since the middle bars and the coupler have an in-plane non-negligible rotational inertia. This approximation is however considered sufficient for our application since it is superior by at least an order of magnitude to existing mechanical watch oscillators that only consist of one rotational inertia and are hence not shaking moment balanced in their plane of oscillation.

2.2. Flexure implementation

Fig. 5 depicts the flexure implementation of the PRBM in Fig. 3. The ideal pivots $\mathbf{P_1}$, $\mathbf{P_2}$, $\mathbf{P_9}$, $\mathbf{P_{10}}$ are embodied by *remote center of compliance* (RCC) flexure pivots 101, 102, 109, 110, respectively. The RCC flexure pivot is a particular case of the crossed flexure pivot [33] whose flexures cross outside of their physical structure, thus presenting an advantageous planar structure. The intersection of the flexures defines (to a first approximation) the axis of rotation of the pivot [32,34]. The two RCC pivots of each Watt oscillator are placed symmetrically so as to compensate the effect of their parasitic center shift [22]. The ideal pivots $\mathbf{P_3}$ to $\mathbf{P_8}$ and $\mathbf{P_{11}}$ to $\mathbf{P_{14}}$ are implemented using *small-length flexural pivots* (SLFP) **103** to **108** and **111** to **114**, respectively [30]. Note that in order to respect the isotropy condition of the IsoSpring, the flexure pivots are designed such that the stiffness of the Wattwins oscillator is the same along its *x* and *y* axes.

This design was implemented in a physical prototype used for experimental validation (Fig. 5b). Its size was chosen to facilitate manipulation (75 mm outer diameter instead of 30 mm in Fig. 4). The flexible part was manufactured by wire electrical discharge machining (EDM) a 1 mm thick Ti–6Al–4V sheet. The inertial bodies were conventionally machined in CuZn39Pb3 brass.

2.3. System for balancing and frequency tuning

Tuning the eigenfrequencies of the Wattwins oscillator while shaking force balancing it is equivalent to being able to independently adjust the inertia corresponding to its two DOFs and the motion of its COM. We will show in Section 3.3.1 that this can be achieved by tuning the moment of inertia and COM position of each outer rigid body (**1**, **2**, **9** and **10**). For this purpose, we devised a system consisting of three rotating eccentric masses per outer rigid body depicted in Fig. 6. For example, by rotating eccentric masses $\mathbf{9_1}$ to $\mathbf{9_3}$, one can modify the COM of the outer rigid body **9** as well as its moment of inertia.

Remark 2.1. One can see on Figs. 5b and 6 that the balance wheels that support the eccentric masses are slightly offset from their counterparts assembled on the other side of the flexure plate. Those hidden balance wheels are centered on the pivots of the outer rigid bodies (**1**, **2**, **9** and **10**) in order to add pure inertia to the system without changing the COM conditions of the oscillator. They also compensate the out-of-plane torques generated by the balancing and frequency tuning system. The balance wheels holding the eccentric masses are offset in order to set to the nominal position the COM of their outer rigid body.

Remark 2.2. Ideally, our prototype (Fig. 5) should be symmetrical with respect to its plane of oscillation to prevent exporting (or being excited by) out-of-plane moments. This symmetry is slightly deteriorated here when the eccentric masses are rotated and their supporting balance wheels are offset. The resulting out-of-plane effects are however considered small and are neglected in the analytical model (Section 3). This asymmetry was chosen in order to facilitate experimental manipulation but could be eliminated in the final embodiment.

2.4. Decomposition into two independent 1-DOF oscillators

Our approach to model the Wattwins oscillator is to decompose it

[3] A mechanism is overconstrained when its mobility obtained through Grübler's formula [31] is less than its actual DOF. This can lead to important and unpredictable variations of the stiffness of flexure mechanisms and stresses in their flexures [32].

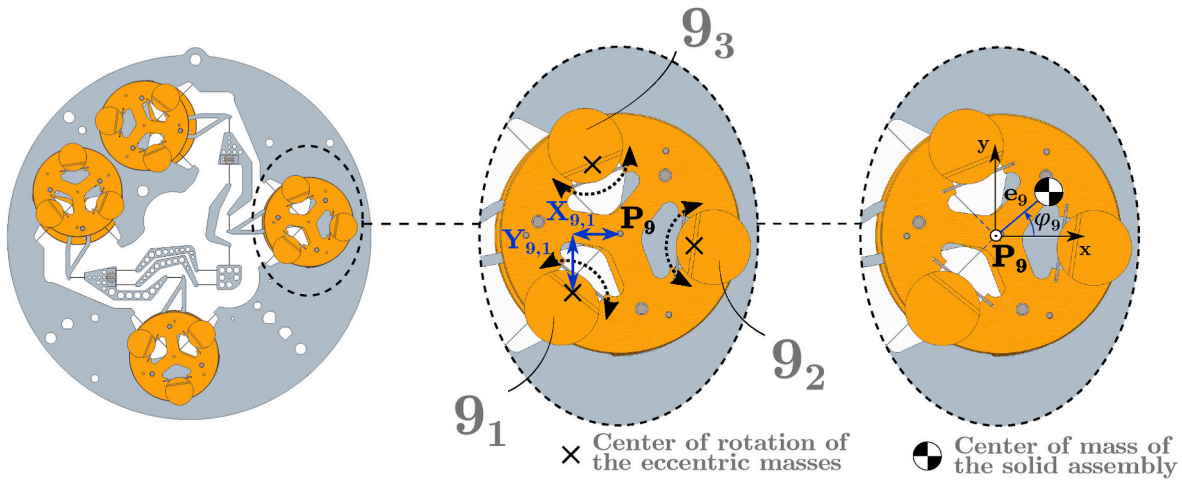

Fig. 6. System for balancing and frequency tuning.

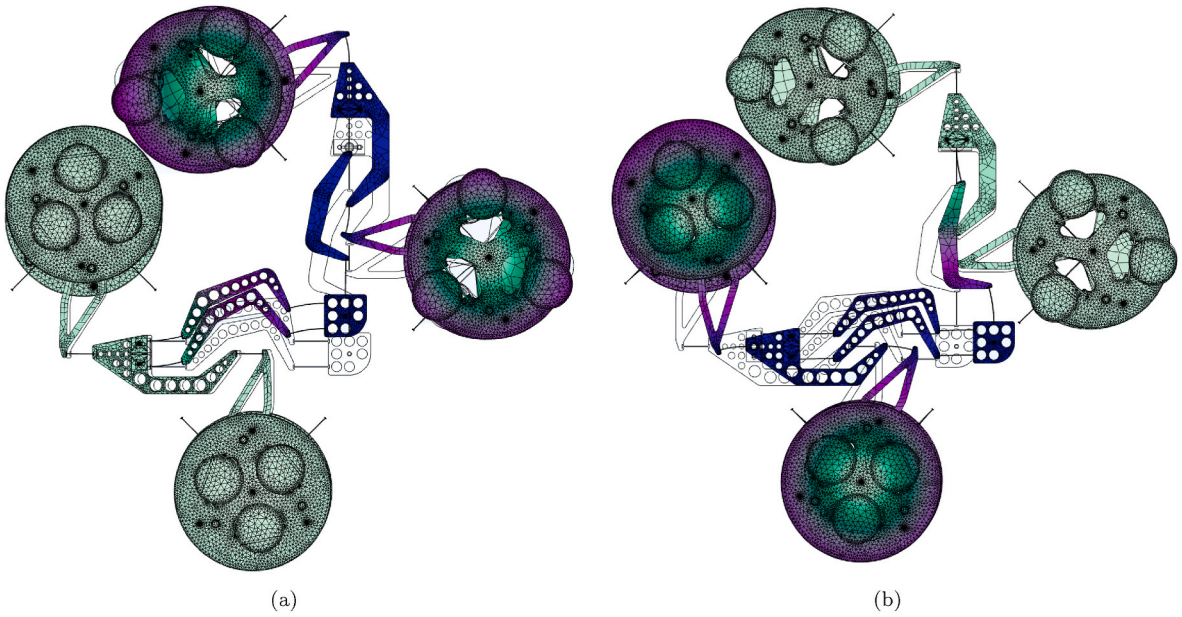

Fig. 7. Wattwins (a) First mode shape (*y*-axis) and (b) Second mode shape (along the *x*-axis) for Setting 1.

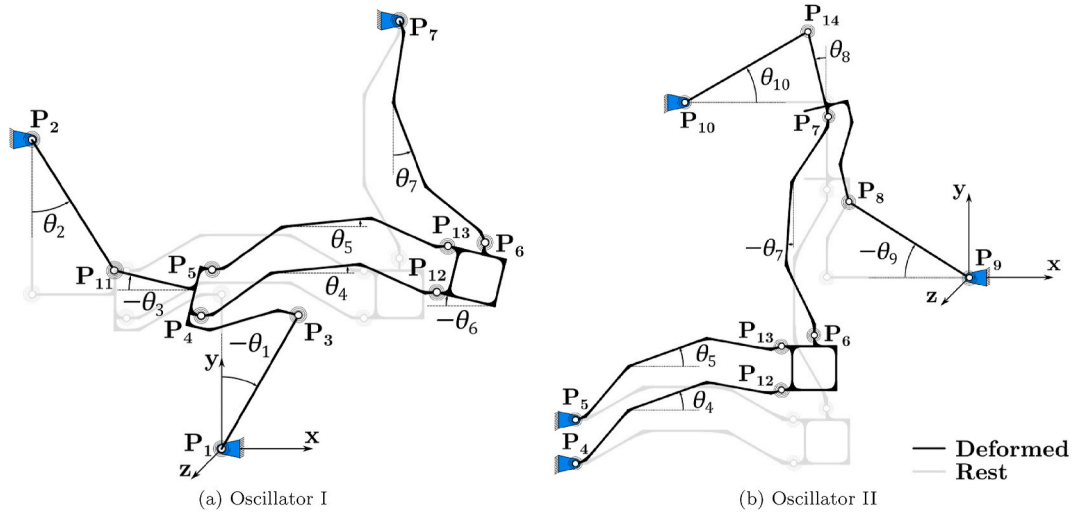

Fig. 8. PRBM of the 1-DOF oscillators I and II in their deformed and rest positions.

into two independent 1-DOF oscillators corresponding to its two first mode shapes. Fig. 7 shows these two mode shapes obtained with the finite element model of the oscillator described in Section 4. One can see that this corresponds, to a first approximation, to blocking the motion of one of the Watt oscillators while letting the other one oscillate freely. The kinematics of these two 1-DOF oscillators, named *Oscillator I* and *Oscillator II*, are depicted in Fig. 8. It is assumed that shaking force balancing each of these independent oscillators and the matching of their eigenfrequencies result in a shaking force balanced Wattwins oscillator with a constant elliptical orbit period.

3. Analytical model

In this section we compute expressions for the eigenfrequencies as well as the COM displacement of oscillators I and II in terms of our tuning parameters which are the inertia and COM position of the four outer rigid bodies (**1**, **2**, **9** and **10**). We then derive the conditions to cancel, up to the second order, the displacement of the COM of each oscillator, hence reaching partial shaking force balancing. We proceed with the following steps:

1. Parameterize the mass properties and kinematics of oscillators I and II.
2. Calculate the kinematic relations between the different angular parameters of oscillators I and II.
3. Calculate the frequencies of oscillators I and II.
4. Calculate the COM displacement of oscillators I and II.
5. Solve the equations of steps 3 and 4 in terms of tuning parameters in order to tune and match the eigenfrequencies of oscillators I and II while shaking force balancing the system.

The analytical model is valid under the following assumptions:

- The transverse stiffnesses of the compliant mechanism are considered infinite compared to its in-plane stiffnesses.
- The rotations are small ($\pm 11.5^\circ$ for the solids **1**, **2**, **4**, **5**, **7**, **9**, **10** and less than 1.8° for the others) and non-linear terms are expressed using series expansions about the rest position.
- The out-of-plane moments generated by the asymmetry of the oscillator with respect to its oscillation plane are negligible. Hence, the flexures are not subjected to shear or torsion and Euler-Bernoulli theory can be used to calculate their stiffness.
- The centers of rotation of the SLFPs are fixed in the middle of the blades.
- The solids connected by flexures are considered infinitely rigid.

3.1. Parameterization

To parameterize the mass properties and kinematics of oscillators I and II, we assign to each rigid body $j = \mathbf{1}$ to **10** a mass m_j, a rotation angle θ_j with respect to its rest position and a local coordinate system located at one of their pivots $\mathbf{P_j}$, see Fig. 8. The local coordinate system of each rigid body is then used to define its COM position with cylindrical coordinates e_j (unit: m) and ϕ_j (unit: rad), its inertia J_j and its translation velocity V_j (at point $\mathbf{P_j}$). Additionally, the rotational stiffness of each flexure pivot $\mathbf{P_j}$ is represented by an ideal torsion spring of stiffness k_j with $j = 1$ to 14.

3.2. Kinematics of oscillators I and II

3.2.1. Oscillator I

The seven angular parameters θ_1 to θ_7 of oscillator I can be identified by projecting along the x and y axes the following loop closure equations, see Fig. 8a

$$\begin{aligned}&\vec{P_1P_3} + \vec{P_3P_{11}} + \vec{P_{11}P_2} + \vec{P_2P_1} = \vec{0}\\ &\rightarrow P_1P_3 + \rightarrow P_3P_5 + \rightarrow P_5P_{13} + \rightarrow P_{13}P_{12} + \rightarrow P_{12}P_4 + \rightarrow P_4P_5 = \vec{0}\\ &+ \rightarrow P_{13}P_6 + \rightarrow P_6P_7 + \rightarrow P_7P_1\\ &= \vec{0}\end{aligned} \tag{4}$$

Following the small amplitudes assumption, we use the Taylor series expansions of trigonometric functions about $\theta_{j\,=\,1,\,\ldots,7} = 0$ to solve the equation system Eq. (4). We then express the angular parameters $\theta_{j\,=\,2,\,\ldots,7}$ in terms of θ_1:

$$\begin{aligned}\theta_2 &= -\theta_1 + \mathcal{O}(\theta_1^3)\\ \theta_3 &= -\frac{H}{L_1}\theta_1^2 + \mathcal{O}(\theta_1^3)\\ \theta_4 &= \frac{(-a^2 + (L_3 - 2c)a + L_1H + 2L_3c)H}{2L_1(L_3 - a)^2}\theta_1^2 + \mathcal{O}(\theta_1^3)\\ \theta_5 &= \theta_4\\ \theta_6 &= \theta_3\\ \theta_7 &= -\frac{H}{L_3 - a}\theta_1 + \frac{1}{2}\frac{(a + 2c)H}{L_1(L_3 - a)}\theta_1^2 + \mathcal{O}(\theta_1^3)\end{aligned} \tag{5}$$

3.2.2. Oscillator II

The seven angular parameters θ_4 to θ_{10} of oscillator II can be identified by projecting along the x and y axes the following loop closure equations, see Fig. 8b

$$\begin{aligned}&\rightarrow P_9P_8 + \rightarrow P_8P_{14} + \rightarrow P_{14}P_{10} + \rightarrow P_{10}P_9\\ &= \vec{0} \rightarrow P_5P_{13} + \rightarrow P_{13}P_{12} + \rightarrow P_{12}P_4 + \rightarrow P_4P_5\\ &= \vec{0} \rightarrow P_9P_8 + \rightarrow P_8P_7 + \rightarrow P_7P_6 + \rightarrow P_6P_{13} + \rightarrow P_{13}P_5 + \rightarrow P_5P_9 = \vec{0}\end{aligned} \tag{6}$$

As in Section 3.2.1, we use the Taylor series expansions of trigonometric functions about $\theta_{j\,=\,4,\,\ldots,10} = 0$ to solve the equation system Eq. (6). We then express the angular parameters $\theta_{j\,=\,4,\,\ldots 8,10}$ in terms of θ_9:

$$\begin{aligned}\theta_4 &= -\frac{H}{L_3 - a}\theta_9 + \mathcal{O}(\theta_9^3)\\ \theta_5 &= \theta_4\\ \theta_6 &= 0\\ \theta_7 &= -\frac{H^2}{2(L_3 - a)^2}\theta_9^2 + \mathcal{O}(\theta_9^3)\\ \theta_8 &= \frac{H}{L_1}\theta_9^2 + \mathcal{O}(\theta_9^3)\\ \theta_{10} &= -\theta_9 + \mathcal{O}(\theta_9^3)\end{aligned} \tag{7}$$

3.3. Frequency tuning of oscillators I and II

Oscillators I and II are based on nearly straight line compliant mechanisms. Hence, we consider them as linear oscillators with an equivalent translation stiffness (unit: N m^{-1}) and an equivalent translation mass (unit: kg) along their observed axis of motion, that is, the x and y axes respectively. In this section, we compute the analytical eigenfrequencies of the oscillators regardless of external perturbations, hence gravity is not considered. The effect of linear accelerations in the plane of oscillation will be dealt with in Section 3.4. In order to calculate the nominal frequencies of the oscillators we derive their motion law using a Lagrangian approach with the following steps:

1. Compute the kinetic energy of oscillators I and II.
2. Compute the potential energy of oscillators I and II.

3. Write the Lagrangian and compute the Euler-Lagrange equation for oscillators I and II in order to extract their motion laws and hence their analytical eigenfrequency.

3.3.1. Kinetic energy of oscillators I and II

The kinetic energies $\mathcal{T}$ of oscillators I and II are

$$\mathcal{T}_I = \frac{1}{2}\sum_{j=1}^{7}\left(J_j\dot{\theta}_j^2 + m_j V_j^2\right) \tag{8}$$

$$\mathcal{T}_{II} = \frac{1}{2}\sum_{j=4}^{10}\left(J_j\dot{\theta}_j^2 + m_j V_j^2\right) \tag{9}$$

where $j = \mathbf{1}\ldots\mathbf{10}$, J_j, θ_j, m_j, V_j are parameters introduced in Section 3.1.

Substituting Eqs. (5) and (7) into Eqs. (8) and (9) and neglecting the higher order terms yields

$$\mathcal{T}_I = \frac{1}{2}\left(J_1 + J_2 + \frac{H^2}{(L_3-a)^2}J_7\right)\dot{\theta}_1^2 + \frac{1}{2}(m_3+m_4+m_5+m_6)H^2\dot{\theta}_1^2 \tag{10}$$

$$\mathcal{T}_{II} = \frac{1}{2}\left(J_9 + J_{10} + \frac{H^2}{(L_3-a)^2}(J_4+J_5)\right)\dot{\theta}_9^2 + \frac{1}{2}(m_6+m_7+m_8)H^2\dot{\theta}_9^2 \tag{11}$$

The inertia of the outer rigid bodies $J_{j\,=\,\mathbf{1,2,9,10}}$ used to compute Eqs. (10) and (11) can be expressed in terms of the rotation angle $\phi_{j,k}$ of the eccentric masses $\mathbf{j_k}$ used to tune the oscillator:

$$J_j = J_{j,cst} + \sum_{k=1}^{3}\left[\left(X_{j,k} + e_{j,k}\cos\phi_{j,k}\right)^2 + \left(Y_{j,k} + e_{j,k}\sin\phi_{j,k}\right)^2\right]m_{j,k} \tag{12}$$

In this equation $J_{j,cst}$ comprises the constant components of the inertia of the outer rigid body j (flexure plate inertia, balance wheel inertia and inertia of the eccentric masses with respect to their own COM). The tunable component of the inertia is function of the mass $m_{j,k}$ of the eccentric masses, the coordinates $X_{j,k}$, $Y_{j,k}$ of their center of rotation (COR) with respect to their respective pivot $\mathbf{P}_j$ and the distance $e_{j,k}$ from their COR to their COM (Fig. 6).

3.3.2. Potential energy of oscillators I and II

Since we do not consider external effects, the total potential energy V_i of oscillators i = I or II is reduced to their elastic potential energy $V_{e,i}$ given by

$$\begin{aligned} V_{e,I} = \frac{1}{2}\big(&k_1\theta_1^2 + k_2\theta_2^2 + k_7\theta_7^2 + k_3(\theta_1-\theta_3)^2 + k_{11}(\theta_2-\theta_3)^2 + k_4(\theta_3-\theta_4)^2 \\ &+ k_5(\theta_3-\theta_5)^2 + k_{12}(\theta_3-\theta_4)^2 + k_{13}(\theta_3-\theta_5)^2 + k_6(\theta_7-\theta_6)^2\big) \end{aligned} \tag{13}$$

$$\begin{aligned} V_{e,II} = \frac{1}{2}\big(&(k_4+k_{12})\theta_4^2 + (k_5+k_{13})\theta_5^2 + k_6\theta_7^2 + k_9\theta_9^2 + k_{10}\theta_{10}^2 + k_{14}(\theta_{10}-\theta_8)^2 \\ &+ k_7(\theta_7-\theta_8)^2 + k_8(\theta_9-\theta_8)^2\big) \end{aligned} \tag{14}$$

Substituting Eqs. (5) and (7) into Eqs. (13) and (14) and neglecting the higher order terms yields

$$V_{e,I} = \frac{1}{2}\left(k_1 + k_2 + k_3 + k_{11} + \frac{H^2}{(L_3-a)^2}(k_6+k_7)\right)\theta_1^2 \tag{15}$$

$$V_{e,II} = \frac{1}{2}\left(k_8 + k_9 + k_{10} + k_{14} + \frac{H^2}{(L_3-a)^2}(k_4+k_5+k_{12}+k_{13})\right)\theta_9^2 \tag{16}$$

The nominal angular stiffnesses $k_{j\,=\,1\ldots14}$ of the RCC flexure pivots and SLFPs can be expressed using the formulas from Cosandier et al. [32]. The angular stiffness of the RCC flexure pivots is

$$k_j = \frac{8EI_j\left(L_2^2 + 3pL_2 + 3p^2\right)}{L_2^3} \quad \text{with } j = 1,2,9 \text{ and } 10 \tag{17}$$

where E is Young's modulus for the flexures, I_j is their area moment of inertia, L_2 is their length and p is the distance between the mobile end of the leaf springs and their intersection axis, see Fig. 5a.

The SLFPs j = 3, 8, 11 and 14 are mainly subjected to bending stress so their angular stiffness can be expressed as

$$k_j = \frac{EI_j}{l} \quad \text{with } j = 3,8,11 \text{ and } 14 \tag{18}$$

where l is the length of flexures 103, 108, 111 and 114, see Fig. 5a.

The SLFPs j = 4, 5, 6, 7, 12 and 13 are subjected to shear and bending stress so their equivalent angular stiffness can be expressed as

$$k_j = \frac{6EI_j\left(1-\frac{\xi}{2}\right)^2}{\xi(3-3\xi+\xi^2)L_3} \quad \text{with } j = 4,5,6,7,12 \text{ and } 13 \tag{19}$$

where a is the length of the flexures 104-107, 112 and 113, L_3 is the length of the coupling solids including the SLFPs' lengths, $\xi = \frac{2a}{L_3}$ is the ratio between the length of the flexure blades and the length of the coupling solids, see Fig. 5a.

3.3.3. Motion laws and frequencies of oscillators I and II

For each oscillator I and II, the Lagrangian is given by

$$\mathcal{L}_i = \mathcal{T}_i - V_i$$

and the Euler-Lagrange equation in θ_j (with j = 1 for i = I and j = 9 for i = II) satisfies

$$\frac{d}{dt}\left(\frac{\partial\mathcal{L}_i}{\partial\dot{\theta}_j}\right) = \frac{\partial\mathcal{L}_i}{\partial\theta_j} \tag{20}$$

Using the results from Eqs. (10), (11), (15) and (16) and considering that for small amplitudes $q_i = -H\theta_j$, Eq. (20) becomes the equation of motion of a simple translation harmonic oscillator

$$m_i\ddot{q}_i + k_i q_i = 0 \tag{21}$$

with

$$\begin{aligned} m_I &= \frac{J_1+J_2}{H^2} + \frac{J_7}{(L_3-a)^2} + m_3 + m_4 + m_5 + m_6 \\ m_{II} &= \frac{J_9+J_{10}}{H^2} + \frac{J_4+J_5}{(L_3-a)^2} + m_6 + m_7 + m_8 \end{aligned} \tag{22}$$

$$\begin{aligned} k_I &= \frac{k_1+k_2+k_3+k_{11}}{H^2} + \frac{k_6+k_7}{(L_3-a)^2} \\ k_{II} &= \frac{k_8+k_9+k_{10}+k_{14}}{H^2} + \frac{k_4+k_5+k_{12}+k_{13}}{(L_3-a)^2} \end{aligned} \tag{23}$$

The eigenfrequency of each 1-DOF oscillator is then found by solving the differential equation (21), yielding

$$f_i = \frac{1}{2\pi}\sqrt{\frac{k_i}{m_i}} \tag{24}$$

The frequency of oscillators I and II can now be tuned by modifying the inertia of the outer rigid bodies $J_{j\,=\,\mathbf{1,2,9,10}}$. This tuning is implemented using the system of eccentric masses depicted in Fig. 6 using Eq. (12) in Section 3.3.1.

3.4. Sensitivity to linear accelerations

In Section 1.4, we announced that in order to study the sensitivity to linear accelerations of our oscillator, the specific case of gravity

sensitivity will be addressed. Indeed, the results from this study can be applied to any linear accelerations.

In order to be gravity insensitive, hence to be insensitive to linear accelerations, the total potential energy of the oscillators over their entire workspace must be independent of gravity orientation. Considering the effect of gravity only in the plane of oscillation, the potential energy of each 1-DOF oscillator i = I or II is

$$V_i = V_{e,i} + V_{g,i} \tag{25}$$

where $V_{e,i}$ is the elastic potential energy given in Eqs. (15) and (16) and

$$V_{g,i} = -M_i \vec{O}\,\vec{G_i} \cdot \vec{g} \tag{26}$$

is the gravitational potential energy. In this last equation, M_i, G_i are the mass and COM position of the oscillator and

$$\vec{g} = g\cos\phi_g \vec{x} + g\sin\phi_g \vec{y} \tag{27}$$

is the gravitational acceleration vector with angle ϕ_g with respect to the x-axis.

In order to satisfy the condition for gravity insensitivity, only the gravitational potential energy of our oscillators must remain constant since their elastic potential is independent from external accelerations. Since we consider all gravity orientations in the plane of oscillation, this means that the COM of oscillators I and II must remain at the same position during oscillation and the condition becomes

$$\frac{d\vec{O}\,\vec{G_i}}{dt} = \vec{0} \tag{28}$$

The COM velocity of each 1-DOF oscillator can be expressed for small displacements in terms of x and y components using the kinematic parameters of Eqs. (5) and (7):

$$\frac{d\vec{O}\,\vec{G_i}}{dt}\cdot\vec{x} = \frac{A_{i,x} + B_{i,x}\theta_j + \mathcal{O}\left(\theta_j^2\right)}{M_i}\dot{\theta}_j \quad \frac{d\vec{O}\,\vec{G_i}}{dt}\cdot\vec{y} = \frac{A_{i,y} + B_{i,y}\theta_j + \mathcal{O}\left(\theta_j^2\right)}{M_i}\dot{\theta}_j \tag{29}$$

with

$$\begin{aligned} A_{i,x} &= -e_j m_j \sin\phi_j + e_{j+1} m_{j+1} \sin\phi_{j+1} + a_{i,x} \\ A_{i,y} &= e_j m_j \cos\phi_j - e_{j+1} m_{j+1} \cos\phi_{j+1} + a_{i,y} \\ B_{i,x} &= -e_j m_j \cos\phi_j - e_{j+1} m_{j+1} \cos\phi_{j+1} + b_{i,x} \\ B_{i,y} &= -e_j m_j \sin\phi_j - e_{j+1} m_{j+1} \sin\phi_{j+1} + b_{i,y} \end{aligned} \tag{30}$$

For each 1-DOF oscillator i = I or II with j = 1 or 9 respectively, e_j and ϕ_j are the COM coordinates of the outer rigid bodies that can be tuned using the eccentric masses of Section 2.3 and $a_{i,x}$, $a_{i,y}$, $b_{i,x}$, $b_{i,y}$ are fixed parameters that depend on the geometrical and mass properties of the oscillator given in Appendix A.

In order to satisfy Eq. (28) for the first two orders, one must have

$$A_{i,x} = A_{i,y} = B_{i,x} = B_{i,y} = 0 \tag{31}$$

This condition can be satisfied by solving the equation system Eq. (30) as function of the tuning parameters, which are the mass properties of the rigid bodies **1**, **2**, **9** and **10**, yielding:

$$\begin{aligned} e_j &= \frac{\sqrt{\left(a_{i,x} + b_{i,y}\right)^2 + \left(a_{i,y} - b_{i,x}\right)^2}}{2m_j} \\ e_{j+1} &= \frac{\sqrt{\left(a_{i,x} - b_{i,y}\right)^2 + \left(a_{i,y} + b_{i,x}\right)^2}}{2m_{j+1}} \\ \phi_j &= arctan2\left(a_{i,x} + b_{i,y}, b_{i,x} - a_{i,y}\right) \\ \phi_{j+1} &= arctan2\left(b_{i,y} - a_{i,x}, a_{i,y} + b_{i,x}\right) \end{aligned} \tag{32}$$

The effect of the COM displacement of a structure on its shaking force balancing can be calculated based on the analytical model. In practice, however, it is more convenient to evaluate the displacement of the COM of a mechanism by measuring indirect effects corresponding to different orders of displacement, see Section 1.3. This is also the approach that is used to validate our models in Section 4. These effects can be seen from the static equilibrium equations of the oscillators obtained by deriving their total potential energy given in Eq. (25):

$$F_i = K_i q_i \tag{33}$$

where

$$F_i = \frac{g}{H}\left(A_{i,x}\cos\phi_g + A_{i,y}\sin\phi_g\right) \tag{34}$$

is the resulting force gravity exerts either along the x-axis of rigid body **3** of oscillator I or along the y-axis of rigid body **8** of oscillator II, and

$$K_i = k_i - \frac{g}{H^2}\left(B_{i,x}\cos\phi_g + B_{i,y}\sin\phi_g\right) \tag{35}$$

is the overall equivalent translation stiffness of oscillators I or II with k_i the nominal translation stiffness in the absence of gravity, see Eq. (23).

One can see that the first order effect of the COM displacement results in an external force F_i exerted by gravity that will cause a *sag* of the oscillator

$$q_{i,sag} = \frac{F_i}{K_i} \approx \frac{F_i}{k_i} \tag{36}$$

since the first order effects dominate. One can thus assess if a compliant mechanism is balanced at first order by measuring the sag of its axes.

Once the sag is cancelled, the second order effect of the COM displacement can be evaluated from the changes in stiffness K_i of the oscillator caused by gravity. One can thus assess if a compliant mechanism is balanced up to second order by measuring its stiffness variation for different orientations of gravity. In practice, this is typically done by measuring the variations of its eigenfrequencies.

3.5. Frequency tuning and shaking force balancing

For each independent oscillator I and II, we derived above expressions to compute the analytical eigenfrequency (one equation per oscillator, see Eq. (24)) and to cancel the COM velocity (four equations per oscillator, see Eq. (32)). We expressed them as functions of our 12 tuning parameters which are the inertias and the x and y coordinates of the COM of the four outer rigid bodies (**1**, **2**, **9**, and **10**) that can be controlled by rotating the eccentric masses of the balancing and frequency tuning system (see Section 2.3). In total, we have 10 equations for 12 tuning parameters. The redundant parameters are tunable inertias of the two oscillators, which means that, for each of them, the same frequency can be reached with different combinations of inertias. Note that these two extra tuning DOFs were introduced in order to solve the two additional equations necessary to reach shaking moment balancing for oscillators I and II, which is out of the scope of this article.

4. Numerical validation

In this section, we validate the analytical model described in Section 3 on the Wattwins oscillator prototype depicted in Fig. 5b by the finite element method (FEM) using the commercial software COMSOL Multiphysics© [35]. The rigid bodies of the oscillator are defined as *Rigid Domains*. The oscillator is meshed with 20-node hexahedral elements that are refined on the flexure with 3 elements across their thickness and 5 elements along their height, see Fig. 9. To reduce computation time, we set 1 element along the height of the *Rigid Domains* when possible. All the structural analyses were done using the geometric non-linearity setting as we are interested in the second order behavior of the oscillator.

All the numerical parameters of the Wattwins oscillator prototype

are grouped in Table B.4, B.5 and B.6 in Appendix B. All the implemented angular settings for the eccentric masses are grouped in Table C.7 and C.8 in Appendix C.

First, we show that our analytical model for frequency tuning based on the independent oscillators I and II is consistent with the simulations on the 2-DOF Wattwins oscillator. Then, we show that the predicted sags (first order effects of COM displacement) of oscillators I and II when subject to gravity match the simulation results on the 2-DOF oscillator. Finally, once the sag is cancelled, we demonstrate that our analytical model can predict the overall stiffness variation (second order effect of COM displacement) of the Wattwins oscillator and that we can adjust it without affecting the frequencies.

4.1. Frequency tuning

The analytical model used to compute the eigenfrequencies of the 2-DOF oscillator is based both on the equivalent translation stiffness and equivalent translation mass calculation of the two 1-DOF oscillators I and II. In a first step, we use static simulations to validate the analytical equivalent translation stiffnesses of the 1-DOF oscillators. Once the analytical stiffness calculations are validated, we use the COMSOL Eigenfrequency study to validate the analytical eigenfrequencies of the 1-DOF oscillators, thus indirectly validating the calculation of their equivalent translation masses.

4.1.1. Stiffness validation

The stiffness of the 2-DOF oscillator for small deformations along the x and y axes is computed in COMSOL by adding a load on the driving pin attached to the rigid body **6** and evaluating its displacements along these axes. Given the numerical parameters in Tables B.4 to B.6 and the flexures analytical stiffness from Eqs. (17), (18) and (19) one can compute the analytical stiffnesses of the 2-DOF oscillator using Eq. (23). Table 1 shows the results for the analytical and numerical stiffnesses of the oscillator I (i.e., Wattwins x-axis stiffness) and the oscillator II (i.e., Wattwins y-axis stiffness). One can see a good match between the analytical and numerical results, which validates this component of our model. The numerical stiffnesses are approximately 2% higher, which can be explained by the pure bending assumption of our model for blades 103, 108, 111 and 114 that are, in practice, slightly subject to shear stress, which increases their effective stiffness.

Remark 4.1. Since all the subsequent results of the numerical validation depend on the stiffness values, we use the numerical values from Table 1 for both the analytical and FEM results so as to validate the other components of the model independently, without propagating the error from the stiffness component of the model.

4.1.2. Frequency tuning validation

To numerically validate the analytical eigenfrequency model, we extract the two first eigenfrequencies of the Wattwins prototype using the COMSOL Eigenfrequency analysis. The analytical and numerical results are compared at two extreme settings, which allow to validate the range of our tuning system and the validity of our analytical model over this range. In Setting 1, the equivalent mass of the oscillator I is at the low end of the tuning range (i.e., the tuning masses are as close together as possible) while the equivalent mass of the oscillator II is at the high end, see Fig. 7. Setting 2 is at the opposite end of the tuning range, where the frequencies of oscillators I and II are respectively the smallest and the greatest.

The results are shown in Table 2. In order to independently validate the equivalent mass component of the analytical model, the numerical stiffness of Section 4.1.1 was used to calculate the analytical frequencies. The differences between analytical and numerical results are below 1% on both axes for both settings. We thus consider this validates both our analytical frequency model and our approach of decomposing the Wattwins mechanism into two independent 1-DOF oscillators.

4.2. Shaking force balancing

4.2.1. Sag

We validated the first order shaking force balancing of the Wattwins oscillator in COMSOL by subjecting it to different gravity orientations $\phi_g = 0^\circ$ to 360°, see Eq. (27), and evaluating the sag of the pin attached to the rigid body **6** along the x and y axes, see Eq. (36). The analytical and

Table 1
Stiffness comparison between analytical model and FEM.

	Analytical	Numerical	Difference (%)
x-axis	27.067 N m^{-1}	27.715 N m^{-1}	2.4
y-axis	27.234 N m^{-1}	27.756 N m^{-1}	1.9

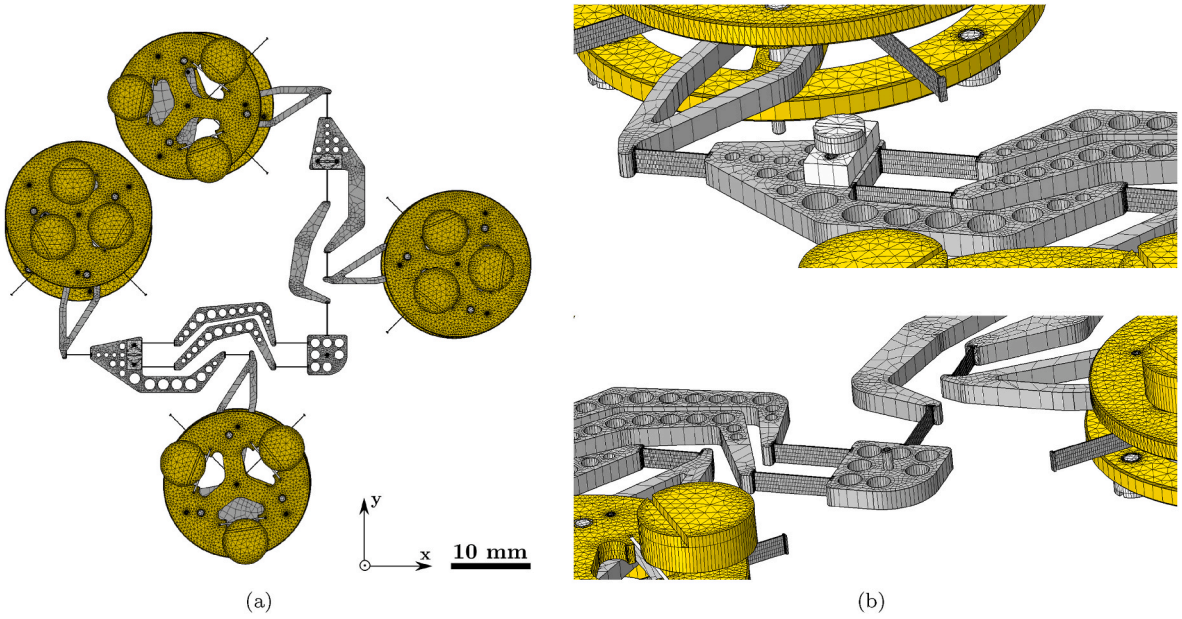

Fig. 9. Wattwins (a) mesh overview and (b) close-up views of the mesh.

numerical results were compared for two settings: Setting 3 that is not balanced and has large sags along the x and y axes and Setting 4 that has been shaking force balanced using our analytical model and hence shouldn't display any sag. Fig. 10 shows a good match between the two models for both settings with a difference within 3% for large sags and a residual error below 1 μm for the balanced setting, which is negligible at the scale of our mechanism.

4.2.2. Stiffness variation

As explained in Section 3.4, once first order balancing has been reached (i.e., the sag of the oscillator has been cancelled), the second order of shaking force balancing has been derived from the stiffness variation of the oscillator when subjected to different orientations of gravity. This was computed in COMSOL by first applying gravity and, once the oscillator has stabilized, imposing a force on the driving pin attached to the rigid body **6** along the studied axis (x or y) and evaluating its displacement along this axis. The stiffness then follows from the force-displacement ratio.

As the Wattwins mechanism is dedicated to horological time bases, it is important to show that its shaking force balancing can be achieved without altering its nominal frequency, which is the frequency that will correspond to civil time. This is shown on Fig. 11 where four different settings were implemented without altering the two eigenfrequencies of the oscillator, matched at $f_0 = 16.75$ Hz. Note that, in order to relate to chronometric performance, the stiffness variations are expressed as *daily rate* ρ, which represents the seconds per day gained or lost with respect to the reference frequency f_0. Assuming the equivalent masses of the oscillator axes to be constant, stiffness is directly linked to its frequency and the definition of daily rate at a frequency f [4]

$$\rho = 86400\frac{f - f_0}{f_0} \tag{37}$$

can be rewritten in terms of stiffness

$$\rho = 86400\frac{\sqrt{k} - \sqrt{k_0}}{\sqrt{k_0}} \tag{38}$$

where k and k_0 are respectively the measured and nominal stiffnesses of the oscillator axes.

Figs. 11a and d compare analytical and FEM results in the case where the analytical model predicts either no second order effects (i.e., partial shaking force balancing) or large second order effects, respectively. The fact that the performance of Setting 4 (which is theoretically perfect) is only a factor of approximately two better than Setting 7 (which theoretically presents defects of ±200 s/day approximately) shows the limit of an open-loop use of the analytical model: the trend of the second order defect can be predicted with an accuracy not better than 100 s/day. We show, however, that our analytical model allows to control independently the sign and magnitude of the stiffness variation for each axis:

- Comparing settings 4 and 5 (Fig. 11a and b) shows that we can modify the magnitude of the daily rate variation (i.e., stiffness variation) of the x-axis without affecting the y-axis,
- Comparing settings 5 and 6 (Fig. 11b and c) shows that we can invert the daily rate variation (i.e., stiffness variation) of the x-axis without affecting the y-axis,
- Comparing settings 5 and 7 (Fig. 11b and d) shows that we can modify the sign and magnitude of the daily rate variation of the y-axis without affecting that of the x-axis.

In summary, even though our analytical is not accurate enough to directly reach shaking force balancing, it can be used iteratively to tune independently the balancing of each oscillation axis and hence find a setting that cancels the effect of gravity without affecting the nominal frequencies set in Section 4.1. This is the main result of this work. The next section explains how to calculate these settings.

4.2.3. Fine tuning

One can see from the results of Figs. 10b and 11a that the residual defects for first and second order effects of gravity have a cosine shape. This means that our analytical model is still valid at this order of magnitude but that the geometric and mass parameters of our system are not estimated accurately enough, see Table B.4. This can be explained by the simplifications of our PRBM, which assumes that the rigid and flexible parts can be clearly separated and that the flexure joints behave as ideal rotational joints with a torsional stiffness, whereas this is not exactly the case in practice.

In order to improve these results, one can still use the developed analytical model to find a new setting based on the residual defect obtained by FEM. The method is to compensate the residual first and second order FEM defects by generating a setting for which the analytical model produces the opposite defects. We proceed with the following steps:

1. Using the residual defect curves for sag $Sag(\phi_g)$ and daily rate $\rho(\phi_g)$ in Figs. 10b and 11a, compute the coefficients $A_{i,x,cor}$, $A_{i,y,cor}$, $B_{i,x,cor}$, $B_{i,y,cor}$ of the opposite curves. These coefficients can be obtained from the results for specific values of ϕ_g:

$$-Sag(\phi_g = 0^\circ) = Sag(\phi_g = 180^\circ) = \frac{g}{Hk_i}A_{i,x,cor}$$

$$-Sag(\phi_g = 90^\circ) = Sag(\phi_g = 270^\circ) = \frac{g}{Hk_i}A_{i,y,cor}$$

$$-\rho(\phi_g = 0^\circ) = \rho(\phi_g = 180^\circ) = 86400\frac{\sqrt{k_i - \frac{g}{H^2}B_{i,x,cor}} - \sqrt{k_i}}{\sqrt{k_i}}$$

$$-\rho(\phi_g = 90^\circ) = \rho(\phi_g = 270^\circ) = 86400\frac{\sqrt{k_i - \frac{g}{H^2}B_{i,y,cor}} - \sqrt{k_i}}{\sqrt{k_i}}$$

2. Using the coefficients from step 1, compute the new COM locations of the outer rigid bodies for each axis $e_{j,cor}$, $\phi_{j,cor}$, $e_{j+1,cor}$, $\phi_{j+1,cor}$ using Eq. (30).
3. Compute the positions of the eccentric masses allowing to obtain the COM coordinates of step 2 without changing the inertia of the outer bars.

Applying our three steps algorithm resulted in the Setting 8 depicted in Fig. 12. This last setting allows to improve the previous results of Setting 4 by an order of magnitude. The residual sag is reduced from approximately ±1 μm to approximately ±10 nm. The daily rate caused by the residual stiffness variation is also reduced from approximately ±100 s/day to a value between +4.6 and −2.7 s/day for both axes.

Table 2
Frequency comparison between analytical model and FEM for Setting 1 and Setting 2.

	Setting 1			Setting 2		
	Analytical	Numerical	Difference (%)	Analytical	Numerical	Difference (%)
x-axis	17.600 Hz	17.459 Hz	0.8	16.318 Hz	16.230 Hz	0.5
y-axis	16.333 Hz	16.222 Hz	0.7	17.551 Hz	17.443 Hz	0.6

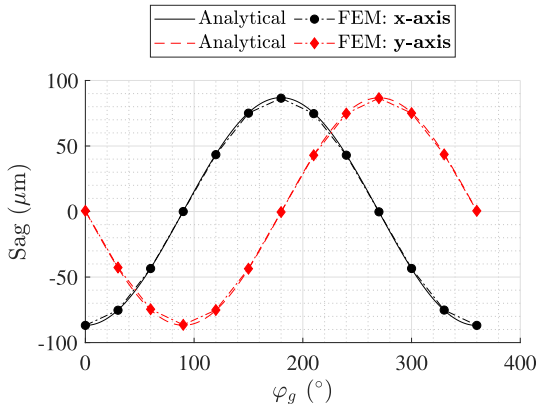

(a) Setting 3:

$A_{I,x} = -3.9 \times 10^{-6}\,\mathrm{kg\,m}$ | $A_{II,x} = 1.9 \times 10^{-8}\,\mathrm{kg\,m}$

$A_{I,y} = 1.1 \times 10^{-8}\,\mathrm{kg\,m}$ | $A_{II,y} = -3.9 \times 10^{-6}\,\mathrm{kg\,m}$

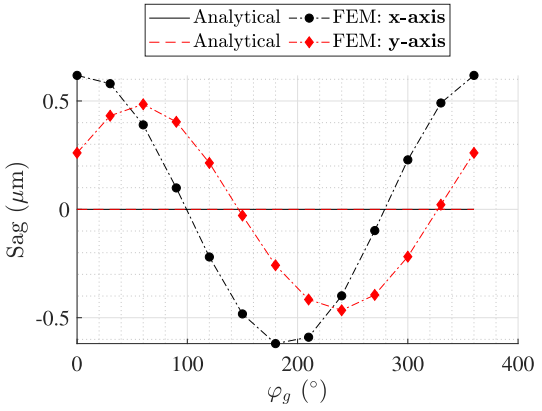

(b) Setting 4:

$A_{I,x} = 2.6 \times 10^{-16}\,\mathrm{kg\,m}$ | $A_{II,x} = 2.4 \times 10^{-20}\,\mathrm{kg\,m}$

$A_{I,y} = 3.2 \times 10^{-16}\,\mathrm{kg\,m}$ | $A_{II,y} = -1.0 \times 10^{-18}\,\mathrm{kg\,m}$

Fig. 10. Sag of the *x* and *y* axes of the Wattwins oscillator with respect to the orientation of gravity for Setting 3 (a) and Setting 4 (b) of the tuning masses.

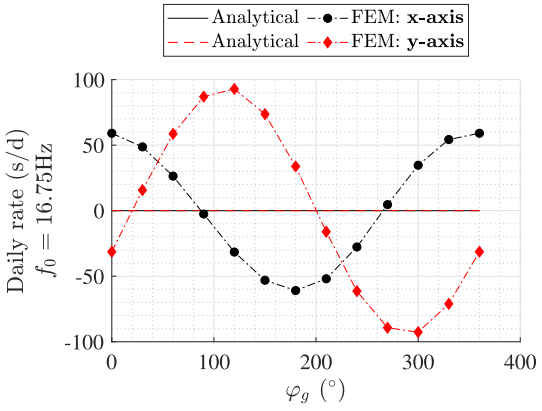

(a) Setting 4:

$A_{I,x} = -1.1 \times 10^{-16}\,\mathrm{kg\,m}$ | $A_{II,x} = 2.4 \times 10^{-20}\,\mathrm{kg\,m}$

$A_{I,y} = 4.1 \times 10^{-17}\,\mathrm{kg\,m}$ | $A_{II,y} = -1.0 \times 10^{-18}\,\mathrm{kg\,m}$

$B_{I,x} = -4.1 \times 10^{-17}\,\mathrm{kg\,m}$ | $B_{II,x} = -1.0 \times 10^{-18}\,\mathrm{kg\,m}$

$B_{I,y} = -1.1 \times 10^{-16}\,\mathrm{kg\,m}$ | $B_{II,y} = 1.2 \times 10^{-20}\,\mathrm{kg\,m}$

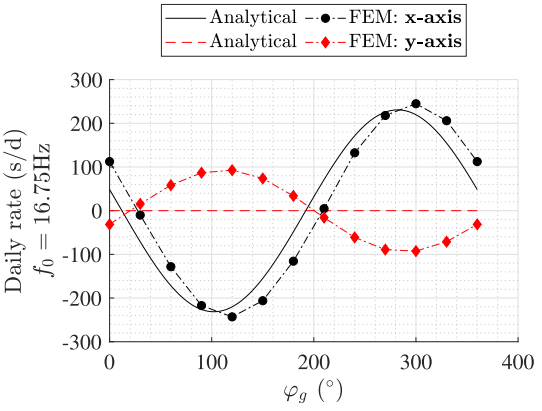

(b) Setting 5:

$A_{I,x} = -5.7 \times 10^{-18}\,\mathrm{kg\,m}$ | $A_{II,x} = 2.4 \times 10^{-20}\,\mathrm{kg\,m}$

$A_{I,y} = 5.2 \times 10^{-17}\,\mathrm{kg\,m}$ | $A_{II,y} = -1.0 \times 10^{-18}\,\mathrm{kg\,m}$

$B_{I,x} = 8.1 \times 10^{-7}\,\mathrm{kg\,m}$ | $B_{II,x} = -1.0 \times 10^{-18}\,\mathrm{kg\,m}$

$B_{I,y} = -3.8 \times 10^{-6}\,\mathrm{kg\,m}$ | $B_{II,y} = 1.2 \times 10^{-20}\,\mathrm{kg\,m}$

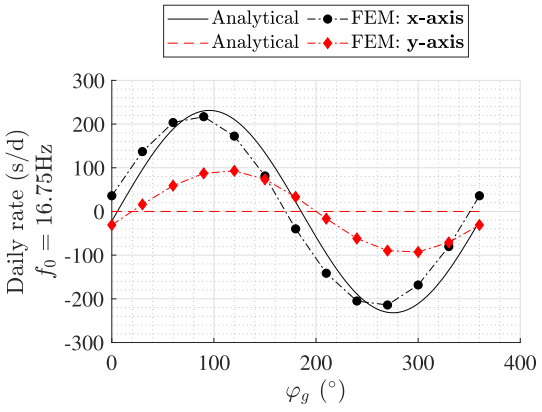

(c) Setting 6:

$A_{I,x} = 1.5 \times 10^{-16}\,\mathrm{kg\,m}$ | $A_{II,x} = 2.4 \times 10^{-20}\,\mathrm{kg\,m}$

$A_{I,y} = -4.7 \times 10^{-16}\,\mathrm{kg\,m}$ | $A_{II,y} = -1.0 \times 10^{-18}\,\mathrm{kg\,m}$

$B_{I,x} = -3.7 \times 10^{-7}\,\mathrm{kg\,m}$ | $B_{II,x} = -1.0 \times 10^{-18}\,\mathrm{kg\,m}$

$B_{I,y} = 3.9 \times 10^{-6}\,\mathrm{kg\,m}$ | $B_{II,y} = 1.2 \times 10^{-20}\,\mathrm{kg\,m}$

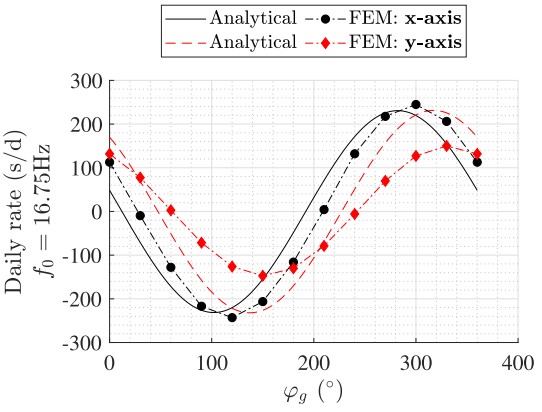

(d) Setting 7:

$A_{I,x} = -5.7 \times 10^{-18}\,\mathrm{kg\,m}$ | $A_{II,x} = 1.2 \times 10^{-18}\,\mathrm{kg\,m}$

$A_{I,y} = 5.2 \times 10^{-17}\,\mathrm{kg\,m}$ | $A_{II,y} = 1.7 \times 10^{-17}\,\mathrm{kg\,m}$

$B_{I,x} = 8.1 \times 10^{-7}\,\mathrm{kg\,m}$ | $B_{II,x} = -0.9 \times 10^{-6}\,\mathrm{kg\,m}$

$B_{I,y} = -3.8 \times 10^{-6}\,\mathrm{kg\,m}$ | $B_{II,y} = -2.6 \times 10^{-6}\,\mathrm{kg\,m}$

Fig. 11. Daily rate in s/day of the *x* and *y* axes of the Wattwins oscillator as a function of the angle ϕ_g of the direction of gravity in the *xy*-plane, for different settings of the tuning masses.

With this fine tuning, the sensitivity of the time base to gravity is well within the 10 s/day variation in daily rate limit specified by official mechanical watch testing organizations to obtain the "Chronometer" certification.[4] This method can also be applied with experimental results instead of FEM simulations so we expect to reach the same level of accuracy with the physical prototype.

Remark 4.2. The sag and stiffness variation of the 2-DOF oscillator in Fig. 12 are no longer of cosine shape, showing that we have reached the limits of this analytical model.

5. Preliminary experimental validation

In this section, we present the first experimental results concerning the shaking force balancing of the titanium Wattwins oscillator prototype. These results are limited to the first order shaking force balancing characterized by the sag of the oscillator under different gravity orientations, see Eq. (36). The experimental validation of the second order shaking force balancing and frequency matching requires the development of dedicated experimental setups and frequency extraction algorithms that are beyond the scope of this article. The preliminary results should however reassure the reader that the theory presented here will not be invalidated by these subsequent experiments.

5.1. Stiffness measurement

As in the numerical validation (Section 4.1.1), the sag of the oscillator for a given level of balancing depends on the stiffness of the oscillator. We hence start by measuring the stiffnesses of the x and y axes of our prototype. These values will then be used for the analytical results in Section 5.2, so as to compare sag results that are independent from stiffness discrepancies.

The setup for measuring the x and y axes stiffnesses of the prototype is shown in Fig. 13. A force sensor (Kistler type 9207) with a sensitivity of approximately -115 μC N^{-1} mounted on a translating micrometric table imposes a displacement to either the middle bar **3** or **8**. This displacement is measured by a linear laser distance sensor (Keyence type LK-H082) with a repeatability of 0.1 μm. The stiffness is then estimated from the slope of a linear regression of the measured force-displacement data, see Fig. 14.

Table 3 compares the expected analytical stiffness and the measured one. Note that the expected stiffness is based on the dimensions specified before manufacturing. The differences are within the limits determined by the tolerances on the flexure dimensions and can hence be attributed to manufacturing defects.

5.2. Shaking force balancing measurement

The experimental setup for the shaking force balancing measurement is shown in Fig. 15. The prototype is mounted on a vertical rotating table whose orientation with respect to gravity is measured by an inclinometer. Two laser displacement sensors measure the sag of the oscillator along the x and the y directions.

Fig. 16 shows the sag of the oscillator for twelve equal angular position increments adding up to a full rotation. The orientation with respect to gravity is defined by the angle ϕ_g between the gravity vector and the x-direction of the oscillator. Error bars indicate the repeatability for five measurements performed in each position.

In order to validate the first order shaking force balancing, two settings are compared: Setting 9 that is not balanced and has large sags (equivalent to Setting 3 in Fig. 10) and Setting 10 that is shaking force balanced according to our analytical model. Fig. 16a shows that the analytical model well predicts the prototype's behavior for large defects, with a difference within 5% for the x-axis sag and 10% for the y-axis sag. In the balanced setting (Fig. 16b), the absolute difference between the results stays of the same order, resulting in a residual sag of the prototype of about ±10 μm. These differences can be attributed to the uncertainty on the flexure dimensions and COM location of the different parts composing the physical oscillator. In fact, only the weights of the physical parts were measured and updated in the analytical model. It is however important to notice that the sag of the prototype has been reduced by almost one order of magnitude thanks to the tuning prescribed by the analytical model: from ±100 μm and ±80 μm for the x and y axes, respectively, to ±15 μm and ±10 μm. This shows that our model provides an effective way of force shaking balancing the Wattwins oscillator up to the first order. We expect to be able to further improve the balancing by using the fine-tuning method validated numerically in Section 4.2.3.

Remark 5.1. Note that the analytical model predicts a non-zero sag for Setting 10 (Fig. 16b). This is due to the fact that exact settings cannot be physically implemented and that the analytical results have hence been adapted to match the physical prototype.

Remark 5.2. Ideally, the numerical results would be compared directly to the experimental ones. This is however complicated since all results depend on the stiffness values, see Remark 4.1. The stiffnesses can easily be adapted in the analytical model to match either the numerical or experimental values. However, matching experimental and numerical models would require artificially changing the dimensions or material properties in the FEM model, which can have side effects. For this reason, we consider that the fit between experimental and FEM results can be indirectly confirmed by comparing them to the analytical results, i.e., comparing Figs. 10 and 16.

6. Conclusion and contributions

In this article, we introduced the Wattwins horological time base, a novel 2-DOF flexure oscillator based on the parallel coupling of two 1-DOF Watt oscillators. For this time base to be compatible with a timekeeper, we showed that we were able to tune independently and match its two eigenfrequencies, as well as make them insensitive to linear accelerations such as gravity, a major source of perturbation for portable timekeepers. This was achieved by developing a new approach to shaking force balancing based on the decomposition of perturbations into effects corresponding to different orders of COM displacement. As a result, the level of shaking force balancing can be tailored to the order of precision required for the application, in our case the second order. This approach is novel and particularly suited to the field of compliant mechanisms, where perfect shaking force balancing significantly increases the complexity of the mechanisms.

We developed a model of the oscillator based on its decomposition into two independent 1-DOF oscillators (I and II) whose kinematics are based on its two first mode shapes. This approach was validated by numerical simulation where we showed that the analytical model correctly predicts the behavior of the 2-DOF oscillator at first and second order. The analytical model did not enable us to reach the desired level of shaking force balancing for our application in a single step but, based on the residual error, the analytical model was able to provide a setting reaching our goal. With this setting, the remaining chronometric error due to gravity is well within 10 s/day, which satisfies typical mechanical watch specifications.

This fine tuning can also be performed on physical prototypes using experimental results: a system of twelve eccentric masses was devised to implement it. Two prototypes were built to validate our concepts: one in titanium at the decimeter scale and one in silicon at the centimeter scale. The silicon prototype served as proof-of-concept: we succeeded in matching its eigenfrequencies and driving it using a watch movement.

[4] See the requirements for the "Chronometer" certificate of the Official Swiss Chronometer Testing Institute (COSC) at www.cosc.swiss/en/certification/mechanical-movements.

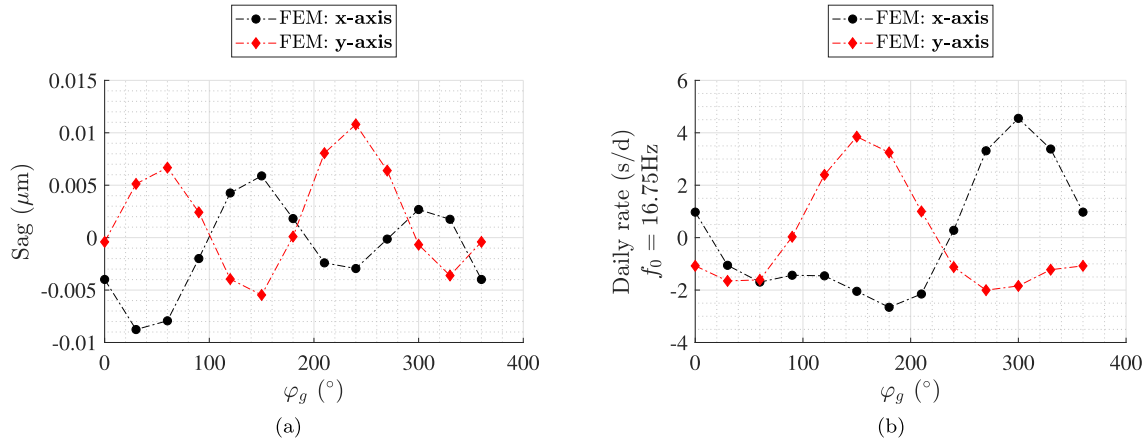

Fig. 12. Setting 8: (a) Residual sag (in μm) and (b) residual gravity stiffness variation (in s d^{-1}) of the x and y axes of the Wattwins oscillator versus the angle ϕ_g of the gravity load in the xy-plane for the corrected setting.

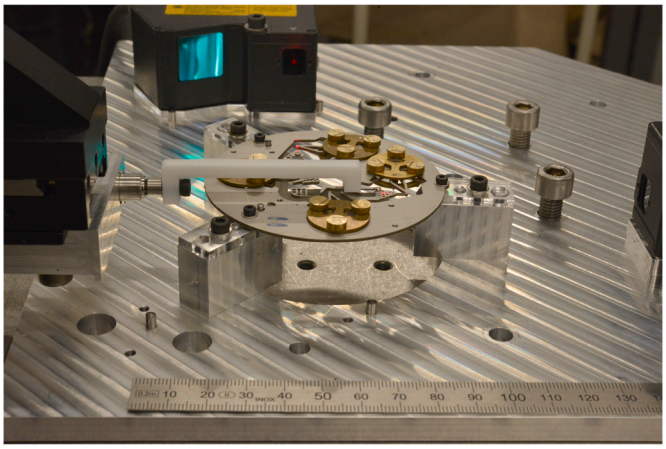

Fig. 13. Stiffness measurement of the y-axis: the force sensor (on the left) pushes the y-axis of the Wattwins oscillator by making contact with the back side of the laser reflector while the Keyence Laser sensor (on the right) measures its displacement.

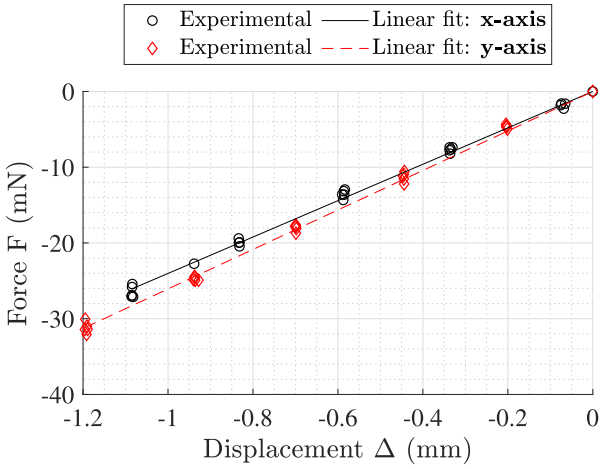

Fig. 14. Experimental stiffness results for the x and y axes of the 2-DOF physical oscillator. The data are fitted with linear regressions: $F_x(\Delta) = 24.023\Delta$ and $F_y(\Delta) = 26.073\Delta$.

Table 3
Stiffness comparison between the analytical model and the physical one.

	Analytical	Experimental	Difference (%)
x-axis	27.067 N m^{-1}	24.023 N m^{-1}	12.7
y-axis	27.234 N m^{-1}	26.073 N m^{-1}	4.5

The titanium prototype allowed to validate experimentally our analytical model for the shaking force balancing at first order and to demonstrate the practicality of our tuning system. The experimental validation of the second order shaking force balancing and frequency matching is beyond the scope of this article and will hence be the topic of future publications. Nevertheless, based on our preliminary results, we expect these experiments to confirm our analytical and numerical results. Our future research will also consist in studying the dynamic balancing of the Wattwins and its isochronism defect, which is a major concern for flexure time bases [2,28,29]. Finally, the out-of-plane gravity effects will be investigated in order to minimize the differences in oscillator frequencies between its horizontal and vertical positions.

To summarize, the main contributions of this article are:

1. A novel Wattwins mechanism design for 2-DOF flexure horological oscillator based on two coupled orthogonal Watt linkages.
2. A new approach to shaking force balancing particularly suited for compliant mechanisms based on the decomposition of perturbations into effects corresponding to different orders of COM displacement.
3. A numerically validated analytical model for the calculation of the eigenfrequencies of the 2-DOF Wattwins oscillator based on two 1-DOF oscillators allowing to independently tune the eigenfrequencies and hence to make them match at a target absolute frequency.
4. A numerically validated analytical model for the shaking force balancing of the Wattwins oscillator up to second order allowing to reach typical mechanical watch chronometric specification.
5. A tuning mechanism comprising twelve eccentric masses allowing to independently tune gravity effects on the two eigenfrequencies of the Wattwins oscillator while matching them to a target frequency.
6. Two Wattwins prototypes at the decimeter and centimeter scales ready for the experimental validation of our theory. They already demonstrated the successful driving of the time base and the practicality of the tuning mechanism.
7. An experimental method to measure the first order shaking force balancing of a Wattwins prototype and the resulting preliminary experimental validation of our theory.

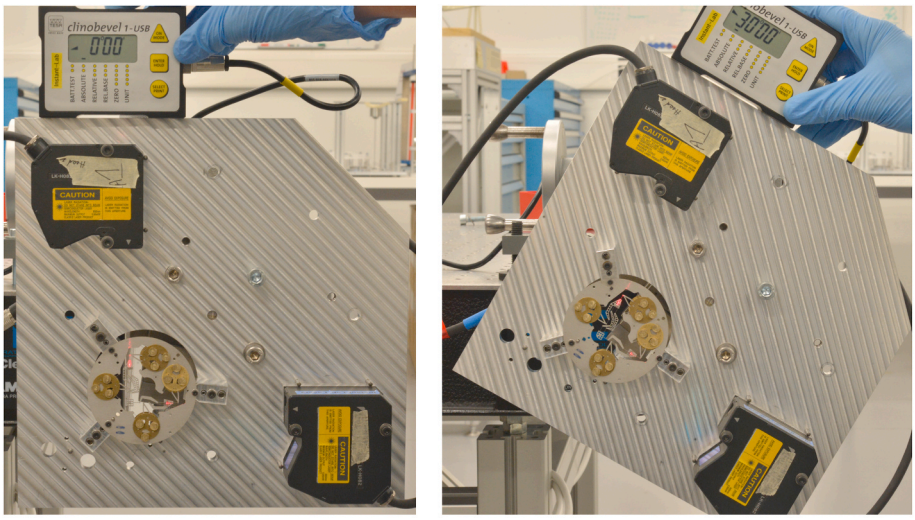

Fig. 15. Titanium Wattwins prototype positioned vertically on its balancing measurement test bench with (a) $\phi_g = 0°$ and (b) $\phi_g = 30°$.

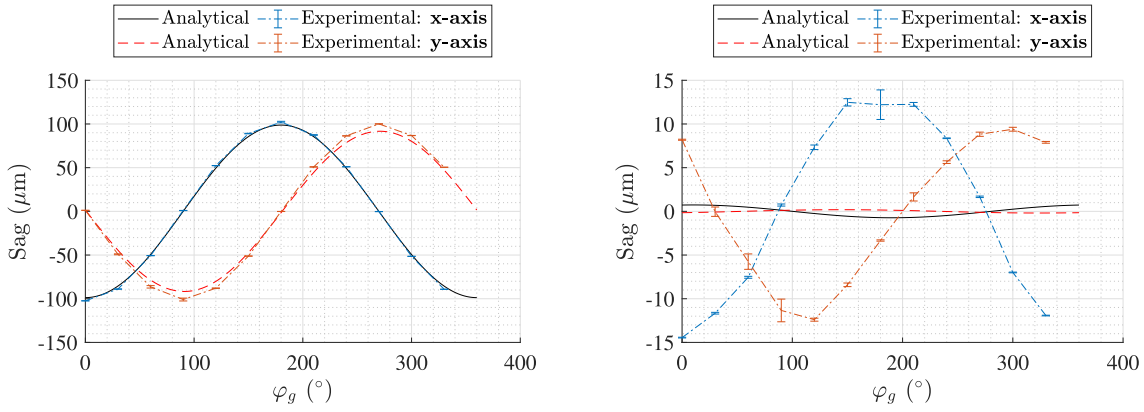

(a) Setting 9:
$A_{I,x} = -3.9 \times 10^{-6}$ kg m | $A_{II,x} = 4.3 \times 10^{-9}$ kg m
$A_{I,y} = 6.4 \times 10^{-8}$ kg m | $A_{II,y} = -3.9 \times 10^{-6}$ kg m

(b) Setting 10:
$A_{I,x} = 2.8 \times 10^{-8}$ kg m | $A_{II,x} = 5.1 \times 10^{-9}$ kg m
$A_{I,y} = -6.6 \times 10^{-9}$ kg m | $A_{II,y} = 4.7 \times 10^{-9}$ kg m

Fig. 16. Sag of the *x* and *y* axes of the titanium Wattwins prototype for two different settings under varying orientations of gravity. The error bars are based on the standard deviation for five measurements per position.

One should note that the Wattwins design is a generic 2-DOF dynamically balanced translation mechanism. It can therefore be used for other applications than horology such as XY high speed robotic manipulators or embedded oscillators on aerospace or other vehicle with high vibration levels.

Declaration of competing interest

The authors declare that they have no known competing financial interests or personal relationships that could have appeared to influence the work reported in this paper.

Acknowledgements

The authors would like to thank the members of the Instant-Lab laboratory who have contributed to the Wattwins conceptual and detailed design: R. Bitterli, L. Convert, T. Fussinger, R. Gillet, M.H. Kahrobaiyan, A. Maurel, B. Nussbaumer and I. Vardi.

Appendix A. Details of the balancing coefficients $a_{i,x}$, $a_{i,y}$, $b_{i,x}$ and $b_{i,y}$

$$a_{I,x} = \frac{H}{L_3 - a}(e_7 m_7 \sin\phi_7 + (-L_3 + a)(m_2 + m_4 + m_5 + m_6)) \tag{A.1}$$

$$a_{I,y} = -\frac{H}{L_3 - a} e_7 m_7 \cos\phi_7 \tag{A.2}$$

$$
\begin{aligned}
b_{I,x} &= \frac{1}{L_1(L_3-a)^2}\big(2e_2m_2(-L_3+a)^2H\sin\phi_2\ldots \\
&-e_4m_4(-Ha^2-2H\left(c-\frac{L_3}{2}\right)a+2cHL_3+H^2L_1)\sin\phi_4\ldots \\
&-e_5m_5(-Ha^2-2H\left(c-\frac{L_3}{2}\right)a+2cHL_3+H^2L_1)\sin\phi_5\ldots \\
&+2e_6m_6(-L_3+a)^2H\sin\phi_6\ldots \\
&+e_7m_7(-L_3+a)(a+2c)H\sin\phi_7\ldots \\
&-e_7m_7H^2L_1\cos\phi_7\ldots \\
&-(-L_3+a)^2H(-m_6a-2m_6c+f(m_4+m_5))\big);
\end{aligned}
\tag{A.3}
$$

$$
\begin{aligned}
b_{I,y} &= \frac{1}{L_1(L_3-a)^2}\big(-2m_2e_2(-L_3+a)^2H\cos\phi_2\ldots \\
&-+e_4m_4(-Ha^2-2H\left(c-\frac{L_3}{2}\right)a+2cHL_3+H^2L_1)\cos\phi_4\ldots \\
&-+e_5m_5(-Ha^2-2H\left(c-\frac{L_3}{2}\right)a+2cHL_3+H^2L_1)\cos\phi_5\ldots \\
&--2e_6m_6(-L_3+a)^2H\cos\phi_6\ldots \\
&--e_7m_7(-L_3+a)(a+2c)H\cos\phi_7\ldots \\
&--\big(m_7e_7\sin\phi_7(H^2)\ldots \\
&-+\big(Hm_2a-Hm_2L_3+m_6H^2)(-L_3+a)\big)L_1\big)
\end{aligned}
\tag{A.4}
$$

$$
a_{II,x} = \frac{H}{L_3-a}(e_4m_4\sin\phi_4+e_5m_5\sin\phi_5) \tag{A.5}
$$

$$
a_{II,y} = \frac{H}{L_3-a}(-e_4m_4\cos\phi_4-e_5m_5\cos\phi_5+(-L_3+a)(m_6+m_7+m_8)); \tag{A.6}
$$

$$
\begin{aligned}
b_{II,x} &= \frac{1}{L_1(L_3-a)^2}\big(-2m_8e_8(-L_3+a)^2H\sin\phi_8\ldots \\
&-\big(m_4H^2e_4\cos\phi_4+m_5H^2e_5\cos\phi_5-m_7H^2e_7\sin\phi_7\ldots \\
&-(-Hm_8L_3\ldots \\
&+Hm_8a+m_6H^2\big)\big(-L_3+a)\big)L_1\big)
\end{aligned}
\tag{A.7}
$$

$$
\begin{aligned}
b_{II,y} &= \frac{1}{L_1(L_3-a)^2}\big(-H^2L_1(e_4m_4\sin\phi_4+e_5m_5\sin\phi_5+e_7m_7\cos\phi_7)\ldots \\
&+2e_8m_8(-L_3+a)^2H\cos\phi_8\big)
\end{aligned}
\tag{A.8}
$$

Appendix B. Geometric and mass parameters for the titanium Wattwins prototype

Table B.4
Ideal Titanium Wattwins prototype: rigid bodies (j) and eccentric masses (j_k) geometric and mass parameters.

J	m_j (kg)	e_j (m)	ϕ_j (rad)	J_j (kg m^2)
1	5.25e-3	**Tunable**	**Tunable**	**Tunable**
2	5.25e-3	**Tunable**	**Tunable**	**Tunable**
3	2.10e-4	1.20e-2	−3.05	3.44e-8
4	7.86e-5	9.32e-3	0.33	8.29e-9
5	8.29e-5	9.37e-3	0.31	8.81e-9
6	7.35e-5	4.42e-3	−1.59	1.75e-9
7	1.16e-4	9.24e-3	−1.85	1.14e-8
8	2.54e-4	1.14e-2	1.44	3.82e-8
9	5.25e-3	**Tunable**	**Tunable**	**Tunable**
10	5.25e-3	**Tunable**	**Tunable**	**Tunable**
j_k	$m_{j,k}$ (kg)	$e_{j,k}$ (m)	$\phi_{j,k}$ (rad)	$J_{j,k}$(kg m^2)
1_1 1_2 1_3	4.58e-4	1.43e-3	**Tunable**	1.85e-9
2_1 2_2 2_3				
9_1 9_2 9_3				
10_1 10_2 10_3				

Table B.5
Physical Titanium Wattwins prototype: rigid bodies (j) and eccentric masses (j_k) geometric and mass parameters.

j	m_j (kg)	e_j (m)	ϕ_j (rad)	J_j (kg m^2)
1	5.33e-3	**Tunable**	**Tunable**	**Tunable**
2	5.27e-3	**Tunable**	**Tunable**	**Tunable**
3	2.07e-4	1.19e-2	−3.04	3.39e-8
4	8.23e-5	9.32e-3	0.33	8.69e-9
5	8.67e-5	9.37e-3	0.31	9.22e-9
6	7.67e-5	4.42e-3	−1.59	1.83e-9
7	1.19e-4	9.24e-3	−1.85	1.19e-8
8	2.53e-4	1.13e-2	1.43	3.79e-8
9	5.32e-3	**Tunable**	**Tunable**	**Tunable**
10	5.30e-3	**Tunable**	**Tunable**	**Tunable**
j_k	$m_{j,k}$ (kg)	$e_{j,k}$ (m)	$\phi_{j,k}$ (rad)	$J_{j,k}$ (kg m^2)
1_1 1_2 1_3	4.60e-4	1.43e-3	**Tunable**	1.86e-9
2_1 2_2 2_3				
9_1 9_2 9_3				
10_1 10_2 10_3				

Table B.6
Titanium Wattwins prototype: gravity constant, Young's modulus, geometric and mass parameters.

Parameter	Value
G (m s^{-2})	9.8066
E_{Ti} (Pa)	114e9
L_1 (m)	20.00e-3
L_2 (m)	11.00e-3
L_3 (m)	20.80e-3
a (m)	4.00e-3
c (m)	2.50e-3
f (m)	3.00e-3
H (m)	16.00e-3
l (m)	3.00e-3
p (m)	0.90e-3
$I_{j\,=\,1,2,9,10}$ (kg m^2)	1.8e-17
$I_{j\,=\,3,8,11,14}$ (kg m^2)	1.8e-17
$I_{j\,=\,4,5,12,13}$ (kg m^2)	1.8e-17
$I_{j\,=\,6,7}$ (kg m^2)	3.52e-17
$X_{1,1}$ (m)	−5.45e-3
$X_{1,2}$ (m)	7.87e-4
$X_{1,3}$ (m)	4.39e-3
$X_{2,1}$ (m)	−4.53e-3
$X_{2,2}$ (m)	5.33e-3
$X_{2,3}$ (m)	−7.75e-4
$X_{9,1}$ (m)	−3.17e-3
$X_{9,2}$ (m)	6.09e-3
$X_{9,3}$ (m)	−1.73e-3
$X_{10,1}$ (m)	6.10e-4
$X_{10,2}$ (m)	1.94e-3
$X_{10,3}$ (m)	−7.27e-3
$Y_{1,1}$ (m)	1.82e-3
$Y_{1,2}$ (m)	−5.95e-3
$Y_{1,3}$ (m)	3.33e-3
$Y_{2,1}$ (m)	−1.93e-3
$Y_{2,2}$ (m)	−5.74e-4
$Y_{2,3}$ (m)	7.29e-3
$Y_{9,1}$ (m)	−4.39e-3
$Y_{9,2}$ (m)	−7.06e-4
$Y_{9,3}$ (m)	5.47e-3
$Y_{10,1}$ (m)	−5.35e-3
$Y_{10,2}$ (m)	4.52e-3
$Y_{10,3}$ (m)	7.41e-4

Appendix C. Implemented settings

Table C.7
Settings 1 to 6.

	Setting 1	Setting 2	Setting 3	Setting 4	Setting 5	Setting 6
$\phi_{1,1}$ ( )	338.77	158.77	270.10	158.77	271.77	82.77
$\phi_{1,2}$ ( )	98.77	278.77	270.10	−81.23	278.77	98.77
$\phi_{1,3}$ ( )	218.77	38.77	270.10	38.77	295.77	104.77
e_1 (m)	3.70e-04	3.70e-04	7.42e-04	3.70e-04	7.27e-04	8.59e-05
ϕ_1 ( )	−97.90	−97.90	−93.88	−97.90	−87.94	179.44
$\phi_{2,1}$ ( )	37.84	217.84	89.58	29.37	−87.53	88.23
$\phi_{2,2}$ ( )	157.84	337.84	89.58	149.37	−63.98	108.59
$\phi_{2,3}$ ( )	277.84	97.84	89.58	−90.63	277.83	89.62
e_2 (m)	1.17e-03	1.17e-03	1.55e-03	1.17e-03	8.15e-04	1.54e-03
ϕ_2 ( )	89.90	89.90	89.82	89.90	84.44	91.23
$\phi_{9,1}$ ( )	231.71	51.71	0.62	51.71	51.71	51.71
$\phi_{9,2}$ ( )	351.71	171.71	0.62	171.71	171.71	171.71
$\phi_{9,3}$ ( )	111.71	291.71	0.62	291.71	291.71	291.71
e_9 (m)	4.51e-04	4.51e-04	8.23e-04	4.51e-04	4.51e-04	4.51e-04
ϕ_9 ( )	9.07	9.07	5.24	9.07	9.07	9.07
$\phi_{10,1}$ ( )	292.30	112.30	179.94	−71.16	−71.16	−71.16
$\phi_{10,2}$ ( )	52.30	232.30	179.94	48.84	48.84	48.84
$\phi_{10,3}$ ( )	172.30	352.30	179.94	168.84	168.84	168.84
e_{10} (m)	1.16e-03	1.16e-03	1.53e-03	1.16e-3	1.16e-03	1.16e-03
ϕ_{10} ( )	−179.27	−179.27	−179.46	−179.27	−179.27	−179.27

Table C.8
Settings 7 to 10.

	Setting 7	Setting 8	Setting 9	Setting 10
$\phi_{1,1}$ ( )	271.77	158.86	−90.57	93.24
$\phi_{1,2}$ ( )	278.77	−142.49	−88.84	−154.84
$\phi_{1,3}$ ( )	295.77	15.82	−88.44	−18.55
e_1 (m)	7.27e-04	3.92e-04	7.45e-4	3.46e-4
ϕ_1 ( )	−87.94	−111.89	−93.54	−98.71
$\phi_{2,1}$ ( )	−87.53	98.00	89.92	−139.25
$\phi_{2,2}$ ( )	−63.98	179.63	88.88	0.17
$\phi_{2,3}$ ( )	277.83	−68.37	87.70	103.37
e_2 (m)	8.15e-04	1.18e-03	1.55e-3	1.21e-3
ϕ_2 ( )	84.44	94.56	89.65	89.85
$\phi_{9,1}$ ( )	307.62	210.00	−0.41	−128.89
$\phi_{9,2}$ ( )	315.62	17.56	−2.07	−3.52
$\phi_{9,3}$ ( )	328.62	−69.93	0.18	119.48
e_9 (m)	7.39e-04	5.04e-04	8.25e-4	4.43e-4
ϕ_9 ( )	−14.08	−8.07	4.58	9.70
$\phi_{10,1}$ ( )	−54.00	173.90	184.19	−67.59
$\phi_{10,2}$ ( )	−32.96	−19.62	183.72	63.77
$\phi_{10,3}$ ( )	318.75	−62.91	181.56	177.65
e_{10} (m)	9.25e-04	1.12e-03	1.53e-3	1.18e-3
ϕ_{10} ( )	−163.31	−172.07	−178.69	−179.38

References

[1] Barrot F, Dubochet O, Henein S, Genequand P, Giriens L, Kjelberg I, Renevey P, Schwab P, Ganny F, Hamaguchi T. Un nouveau régulateur mécanique pour une réserve de marche exceptionnelle. Actes de la Journée d'Etude de la Société Suisse de Chronométrie; 2014. p. 43–8.

[2] Thalmann EFG. Flexure pivot oscillators for mechanical watches. 2020. p. 173. https://doi.org/10.5075/epfl-thesis-8802.

[3] Vardi I. Le facteur de qualité en horlogerie mécanique75; 2014. p. 9.

[4] Reymondin C, Monnier G, Bandi-Tebbutt R, Jeanneret D, Pelaratti U. The theory of horology. Swiss Federation of Technical Colleges; 1999, ISBN 978-2-940025-12-1.

[5] Henein S, Vardi I, Rubbert L, Bitterli R, Ferrier N, Fifanski S, Lengacher D. IsoSpring : vers la montre sans échappement. 2014. p. 10.

[6] Rubbert L, Bitterli R, Ferrier N, Fifanski S, Vardi I, Henein S. Isotropic springs based on parallel flexure stages. Precis Eng 2016;43:132–45. https://doi.org/10.1016/j.precisioneng.2015.07.003. ISSN 01416359.

[7] Newton I. The mathematical principles of natural philosophy, vol. I; 1729. B. Motte, translated by Andrew Motte.

[8] Schneegans H, Thalmann E, Henein S. Driven Wattwins, a 2-DOF isotropic horological oscillator. 2020. https://doi.org/10.5281/zenodo.4309695.

[9] Schneegans H. Statically and dynamically balanced oscillator based on Watt's linkage, 2020-06-12. In: 20th international conference of the European society for precision engineering and nanotechnology (EUSPEN); 2020. Geneva,CH.

[10] Vardi I, Rubbert L, Bitterli R, Ferrier N, Kahrobaiyan M, Nussbaumer B, Henein S. Theory and design of spherical oscillator mechanisms. Precis Eng 2018;51:499–513. https://doi.org/10.1016/j.precisioneng.2017.10.005. ISSN 01416359.

[11] van der Wijk V, Herder JL, Demeulenaere B. Comparison of various dynamic balancing principles regarding additional mass and additional inertia. J Mech Robot 2009;1(4):1942–4310. https://doi.org/10.1115/1.3211022. 041006, ISSN 1942-4302.

[12] Wei B, Zhang D. A review of dynamic balancing for robotic mechanisms. Robotica 2021;39:55–71. https://doi.org/10.1017/S0263574720000168. ISSN 0263-5747, 1469-8668.

[13] Lowen G, Berkof R. Survey of investigations into the balancing of linkages. J Mech 1968;3(4):221–31. https://doi.org/10.1016/0022-2569(68)90001-3. ISSN 00222569.

[14] Arakelian V. Balancing of linkages and robot manipulators: advanced methods with illustrative examples, vol. 27. Cham: Springer; 2015. https://doi.org/10.1007/978-3-319-12490-2. 978-3-319-12490-2 978-3-319-12489-6, of Mechanisms and Machine Science.

[15] Weeke SL, Tolou N, Semon G, Herder JL. A fully compliant force balanced oscillator. In: Volume 5A: 40th mechanisms and robotics conference. Charlotte,

North Carolina, USA: American Society of Mechanical Engineers; 2016, ISBN 978-0-7918-5015-2. https://doi.org/10.1115/DETC2016-59247. V05AT07A008.
[16] Berkof RS, Lowen GG. A new method for completely force balancing simple linkages. J. Eng. Ind. 1969;91(1):21–6. https://doi.org/10.1115/1.3591524. ISSN 0022-0817.
[17] Martinez S, Meijaard JP, van der Wijk V. On the shaking force balancing of compliant mechanisms. In: 2019 7th international conference on control, mechatronics and automation (ICCMA). Delft, Netherlands: IEEE; 2019, ISBN 978-1-72813-787-2. p. 310–4. https://doi.org/10.1109/ICCMA46720.2019.8988681.
[18] Martini A, Troncossi M, Rivola A. Algorithm for the static balancing of serial and parallel mechanisms combining counterweights and springs: generations, assessment and ranking of effective design variants. Mech Mach Theor 2019;137:336–54. https://doi.org/10.1016/j.mechmachtheory.2019.03.031.
[19] Carricato M, Gosselin C. A statically balanced Gough/Stewart-type platform: conception, design and simulation. J Mech Robot 2009;1:031005. https://doi.org/10.1115/1.3147192.
[20] Lu Q, Ortega C, Ma O. Passive Gravity Compensation Mechanisms: Technologies and Applications5; 2011. p. 32–44. https://doi.org/10.2174/1872212111105010032. ISSN 18722121.
[21] Radaelli G, Gallego JA, Herder JL. An Energy Approach to Static Balancing of Systems with Torsion Stiffness133; 2011. p. 1528–9001. https://doi.org/10.1115/1.4004704. 091006, ISSN 1050-0472.
[22] Kahrobaiyan MH, Thalmann E, Rubbert L, Vardi I, Henein S. Gravity-Insensitive Flexure Pivot Oscillators140; 2018. p. 1528–9001. https://doi.org/10.1115/1.4039887. 075002, ISSN 1050-0472.
[23] Tricamo SJ, Lowen GG. A new concept for force balancing machines for planar linkages. Part 2: application to four-bar linkage and experiment. ASME. J. Mech. Des. 1981;103:784–92. https://doi.org/10.1115/1.3254988. ISSN 0161-8458.
[24] P. T. Oortwijn, Fine tuning of a force balanced 1-DoF rotating mechanism ..
[25] Van der Wijk V, Herder JL. Active dynamic balancing unit for controlled shaking force and shaking moment balancing. In: Volume 2: 34th annual mechanisms and robotics conference, parts A and B, ASME 2010 international design engineering technical conferences and computers and information in engineering conference. Montreal, Quebec, Canada: ASMEDC; 2010, ISBN 978-0-7918-4410-6. p. 1515–22. https://doi.org/10.1115/DETC2010-28423.
[26] Van der Wijk V, Krut S, Pierrot F, Herder JL. Design and Experimental Evaluation of a Dynamically Balanced Redundant Planar 4-RRR Parallel Manipulator32; 2013. p. 744–59. https://doi.org/10.1177/0278364913484183. ISSN 0278-3649, 1741-3176.
[27] Hetzel M. Le diapason et son influence sur l'horlogerie. Bulletin Annuel de La Société Suisse de Chronométrie IV– 1962;1962:666–79.
[28] Thalmann E, Kahrobaiyan MH, Vardi I, Henein S. Flexure pivot oscillator with intrinsically tuned isochronism. 075001 J Mech Des 2020;142(7):1528–9001. https://doi.org/10.1115/1.4045388. ISSN 1050-0472.
[29] Thalmann E, Henein S. Design of a flexure rotational time base with varying inertia. J Mech Des 2021;143:1528–9001. https://doi.org/10.1115/1.4050558. 115001, ISSN 1050-0472.
[30] Howell LL. Compliant mechanisms. New York: Wiley; 2001, ISBN 047138478X. 9780471384786.
[31] Grübler M. Getriebelehre: Eine Theorie Des Zwanglaufes Und der Ebenen mechanismen. Berlin Heidelberg: Springer-Verlag; 1917.
[32] F. Cosandier, S. Henein, M. Richard, L. Rubbert, The art of flexure mechanism design URL http://infoscience.epfl.ch/record/232450.
[33] Wittrick W. The theory of symmetrical crossed flexure pivots. Aust J Chem 1948;1:121–34. https://doi.org/10.1071/CH9480121c.
[34] Haringx JA. The cross-spring pivot as a constructional element. Appl Sci Res 1949;1(1):1573–987. https://doi.org/10.1007/BF02120338. 313, ISSN 1386-6184.
[35] COMSOL Multiphysics®. Release 5.4, www.comsol.com; 2019. 11-14.